NAVAL POSTGRADUATE SCHOOL

MONTEREY, CALIFORNIA

THESIS

IMPROVED ATOM INTERFEROMETER PERFORMANCE USING COUNTERINTUITIVE STIMULATED RAMAN ADIABATIC PASSAGE

by

Branden Tatasciore

December 2020

Thesis Advisor: Francesco A. Narducci
Second Reader: Jeffrey G. Lee

THIS PAGE INTENTIONALLY LEFT BLANK

REPORT DOCUMENTATION PAGE			*Form Approved OMB No. 0704-0188*

1. AGENCY USE ONLY *(Leave blank)*	**2. REPORT DATE** December 2020	**3. REPORT TYPE AND DATES COVERED** Master's thesis

4. TITLE AND SUBTITLE IMPROVED ATOM INTERFEROMETER PERFORMANCE USING COUNTERINTUITIVE STIMULATED RAMAN ADIABATIC PASSAGE	**5. FUNDING NUMBERS** RPP86
6. AUTHOR(S) Branden Tatasciore	
7. PERFORMING ORGANIZATION NAME(S) AND ADDRESS(ES) Naval Postgraduate School Monterey, CA 93943-5000	**8. PERFORMING ORGANIZATION REPORT NUMBER**
9. SPONSORING / MONITORING AGENCY NAME(S) AND ADDRESS(ES) IWS6, Washington Navy Yard, Washington DC, 20376	**10. SPONSORING / MONITORING AGENCY REPORT NUMBER**

11. SUPPLEMENTARY NOTES The views expressed in this thesis are those of the author and do not reflect the official policy or position of the Department of Defense or the U.S. Government.

12a. DISTRIBUTION / AVAILABILITY STATEMENT Approved for public release. Distribution is unlimited.	**12b. DISTRIBUTION CODE** A

13. ABSTRACT (maximum 200 words)

Atom interferometers depend on light/matter interactions and are extremely sensitive sensors capable of being employed as accelerometers, rotation sensors, and gravity and magnetic gradiometers. Typical interferometers use a well-known velocity (generally from atoms launched out of an atomic trap) to interferometrically measure quantities of interest (e.g., acceleration and rotation). This thesis evaluates the effects of atom velocity in an atom interferometer sensor that exists at NPS, which uses a continuous beam of cold rubidium atoms with a narrow but not monochromatic range of velocities passing through continuous laser fields. The atom's velocity dictates the interaction time between the atom and laser. However, this combination results in pulse errors due to velocity averaging. One method to counteract these pulse errors uses the so-called counterintuitive laser arrangement—a method known as stimulated Raman adiabatic passage (STIRAP). STIRAP will be shown to be a more robust approach. Starting with the atoms in one of the ground states, all or a portion of the atoms can be transferred to the other ground state in a well-controlled manner. Changes in acceleration and rotation can be sensed with very high precision by a detection laser resulting in applicability as a highly sensitive accelerometer or gyroscope. This project explores experimentally and theoretically the utility of counterintuitive pulse sequences for atom interferometry applications.

14. SUBJECT TERMS stimulated Raman adiabatic passage, STIRAP, atom interferometry, inertial navigation	**15. NUMBER OF PAGES** 93
	16. PRICE CODE

17. SECURITY CLASSIFICATION OF REPORT	**18. SECURITY CLASSIFICATION OF THIS PAGE**	**19. SECURITY CLASSIFICATION OF ABSTRACT**	**20. LIMITATION OF ABSTRACT**
Unclassified	Unclassified	Unclassified	UU

NSN 7540-01-280-5500 Standard Form 298 (Rev. 2-89) Prescribed by ANSI Std. 239-18

THIS PAGE INTENTIONALLY LEFT BLANK

Approved for public release. Distribution is unlimited.

IMPROVED ATOM INTERFEROMETER PERFORMANCE USING COUNTERINTUITIVE STIMULATED RAMAN ADIABATIC PASSAGE

Branden Tatasciore
Lieutenant, United States Navy
BSME, University of New Mexico, 2014

Submitted in partial fulfillment of the
requirements for the degree of

MASTER OF SCIENCE IN APPLIED PHYSICS

from the

NAVAL POSTGRADUATE SCHOOL
December 2020

Approved by: Francesco A. Narducci
Advisor

Jeffrey G. Lee
Second Reader

Kevin B. Smith
Chair, Department of Physics

THIS PAGE INTENTIONALLY LEFT BLANK

ABSTRACT

Atom interferometers depend on light/matter interactions and are extremely sensitive sensors capable of being employed as accelerometers, rotation sensors, and gravity and magnetic gradiometers. Typical interferometers use a well-known velocity (generally from atoms launched out of an atomic trap) to interferometrically measure quantities of interest (e.g., acceleration and rotation). This thesis evaluates the effects of atom velocity in an atom interferometer sensor that exists at NPS, which uses a continuous beam of cold rubidium atoms with a narrow but not monochromatic range of velocities passing through continuous laser fields. The atom's velocity dictates the interaction time between the atom and laser. However, this combination results in pulse errors due to velocity averaging. One method to counteract these pulse errors uses the so-called counterintuitive laser arrangement—a method known as stimulated Raman adiabatic passage (STIRAP). STIRAP will be shown to be a more robust approach. Starting with the atoms in one of the ground states, all or a portion of the atoms can be transferred to the other ground state in a well-controlled manner. Changes in acceleration and rotation can be sensed with very high precision by a detection laser resulting in applicability as a highly sensitive accelerometer or gyroscope. This project explores experimentally and theoretically the utility of counterintuitive pulse sequences for atom interferometry applications.

THIS PAGE INTENTIONALLY LEFT BLANK

Table of Contents

List of Figures

List of Acronyms and Abbreviations

DoD	Department of Defense
NPS	Naval Postgraduate School
USN	U.S. Navy
USG	United States government
2D-MOT	two-dimensional magneto-optical trap
AIG	atomic interferometer gyroscope
AMO	atomic, molecular, and optical physics
AOM	acousto-optic modulator
FWHM	full width at half maximum
GPS	global positioning system
HWPs	half-wave plates
INSs	inertial navigation systems
LIA	lock-in amplifier
MOT	magneto-optical trap
NMR	nuclear magnetic resonance
PBS	polarizing beam-splitting cube
PMT	photomultiplier tube
QWP	quarter-wave plate
RF	radio frequency
RLG	ring laser gyroscope
STIRAP	stimulated Raman adiabatic passage

THIS PAGE INTENTIONALLY LEFT BLANK

Acknowledgments

I would like to thank the Navy for giving me this opportunity to complete this degree. I am very grateful for the help of my advisor, Dr. Frank Narducci. He was able to simplify some of the more difficult topics down to my level of understanding, helping me to finish this project. CDR Michael Manicchia and Dr. Jeff Lee were very instrumental in my progress in the lab. They both were able to navigate me through all the nuances of experimental physics. I am grateful for the opportunity to attend the Naval Postgraduate School and conduct this research. Finally, I would like to acknowledge my wife, Jennifer, and our children, Easton, Emma, and Evelyn, for their love and support throughout this process.

THIS PAGE INTENTIONALLY LEFT BLANK

CHAPTER 1:
Gyroscopes

1.1 Introduction

Safe navigation is of immense importance to every sailor or airmen traversing the planet's seas and skies. Real-time positioning has become as integral part of maintaining that safety and effectively carrying out missions around the world. The Global Positioning System (GPS) has become far and above the standard for use in determining up to the minute position with an accuracy approaching a few meters. GPS is so popular that it has been integrated into nearly every phone and automobile around the world. The military relies on GPS to plan and execute time sensitive missions vital to national security. It is used on board ships, aircraft, and land vehicles as a tool to navigate terrain unfamiliar to the men and women volunteering to enter hazardous regions of the world. Military officials have said the capabilities of GPS were important factors in the outcomes of recent operations such as Desert Storm and Desert Shield. Due to its apparent significance, it has been widely accepted that the GPS infrastructure would be one of the first priority targets by an adversary attempting to cripple the nation and military [1].

For this reason, every naval vessel, aircraft and large-scale missile has self-contained inertial navigation systems (INS) comprising of accelerometers, gyroscopes and computers. The measurements of speed and heading are determined by integrating the outputs of gyroscopes and accelerometers over short periods of time. An additional integration step provides location from a known initial point. However, modern accelerometers and gyroscopes have their own limitations. Imperfections in manufacturing and software round off error introduce errors in the calculation when determining ship's positioning. These sensors are often sensitive to things other than rotation and acceleration. For example, the resonant frequency of a Ring Laser Gyroscope is temperature sensitive. This results in a displacement error from the inertial navigation provided position and the GPS fix. The actual position is different from the display on the computer which could be have disastrous consequences. The inertial system must be periodically updated with GPS information to correct these errors and provide more accurate ship's position. Many people are researching ways to limit these errors, therefore reducing the frequency of GPS updates. Atomic-based gyroscopes have been proven to be a viable replacement as they are far more precise and less susceptible to errors and drifts of the kind just described compared to current commercial systems. For this reason, atomic gyroscopes are of significant interest to the navy as options for safe navigation in GPS compromised

environments.

1.2 Current Technology

Many types of gyroscopes are available for commercial and military use with varying cost and sensitivity depending on the application. Gyroscopic sensors are all designed with the purpose of determining rotation rate of a system when compared to an inertial frame. There is value in refining the precision of such a sensor. A reduction in error could relieve some of the dependence on GPS as navigation teams would depend more on their platform-based systems. This chapter is not designed to cover all the intricacies of each design. It is to introduce a baseline for the typical system found on most naval vessels. This baseline is the ring laser gyroscope (RLG). RLGs are a well-established portion of inertial navigation systems on board navy vessels. Modern versions are known as RLGN, where the N references Navigation grade, are used on submarines to navigate beneath the surface of the ocean, cutoff from GPS satellite communication. These sensors rely on the Sagnac effect to determine rotation rate. Two counter-propagating lasers travel around a closed path starting from the same originating point. Without any inertial change to the system, both lasers will travel around a closed loop in the same amount of time given by $t = \frac{2\pi r}{c}$. Since each beam has the same travel time, there is no change in phase between the two signals corresponding to no sensor rotation. As the sensor rotates, the length of the path of the similarly rotating laser beam appears longer while to the other laser the path appears shorter as seen in Figure 1.1.

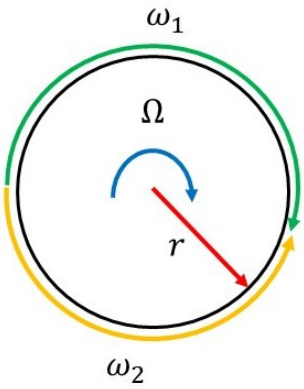

Figure 1.1. A rotating gyro with two counter-propagating laser beams. The path lengths differ due to the rotation causing a phase difference between the two beams at the recombination point and thus an interference pattern.

The difference in propagation time can be expressed as [2]

$$\Delta t = \frac{4\pi r^2 \Omega}{c^2 - r^2\Omega^2}. \tag{1.1}$$

The physical size of the sensor, r, and the rotation rate, Ω, cause the second term in the denominator to be negligible, which simplifies the equation. Simplifying the above equation and solving for phase differences, a relationship for phase change can be found. This change in phase can be compared to the reference frame to determine rotation direction and magnitude [2]. This new equation is given as

$$\Delta\phi = \frac{8\pi^2 r^2 \Omega}{c\lambda}, \tag{1.2}$$

where $\Delta\phi$ is the phase difference between the two different paths. The Sagnac effect results in a change in the path length of one laser beam relative to the other when the ring laser cavity is rotated. A change in path length between the two beams create a circumstance where the two beams now have different phase shifts. In the laboratory, it is easier to measure a frequency. In an active laser gyroscope, the same effect results in two laser modes, f_{cw} and f_{ccw}. Rate detection is based on the change in frequency. The fundamental relationship to define the operation of a basic rotation sensor

is [3]

$$f_{ccw} - f_{cw} = \Delta f = \frac{4A}{\lambda L}\Omega, \tag{1.3}$$

where Δf is the frequency difference, A is the closed optical path area, λ is the laser wavelength, and L is the closed optical path length. Software is used to analyze the change in frequency between the two paths and combined with other sensors convey a ship's position, and orientation. The lives of the men and women on board rely on the accuracy of these sensors. Tremendous study has occurred in the field of gyroscopes and the inherent limitations of these precision sensors. The following section briefly introduces some of those limitations to better understand the continued need for research in this field.

1.3 Limitations

In theory, the principles of INS are simple; they are not, however, perfect. Position errors can accumulate quickly due to errors of system's sensors. Modern technology has brought new, faster, more capable accelerometers. However, even with these advancements, the mechanical and optical gyroscopes have slowed their improvement over the past decade. When long-term inertial navigation is required; such as for a submerged submarine or autonomous drone, the position errors accumulate causing navigational problems [4]. Here are a few examples of errors leading to the problems in performance.

1.3.1 Sensitivity

This thesis investigates ways to drastically increase the sensor's sensitivity. RLGs are fundamentally limited by the effective mass of the photons as the laser travels around the cavity. It will be shown that the sensitivity of the sensor scales with the mass of the photon. This research does not change the mass of the photon but replaces the light photons with heavy atoms. The measurable parameter of these sensors is the phase shift produced by an acceleration or rotation. In terms of rotation only, it has been shown that $\Delta\phi$, the phase shift associated with a rotating atom interferometer, can be expressed as [5], [6]

$$\Delta\phi = \frac{2m}{\hbar}\boldsymbol{\Omega}\boldsymbol{A}, \tag{1.4}$$

where m is the mass of the photon or atom, $\hbar$ is the reduced Planck's constant, $\boldsymbol{\Omega}$ is the rotation vector, and $\boldsymbol{A}$ is the enclosed area (a vector) of the interferometer. We can rewrite Equation 1.4 by

solving for minimum detectable rotation rate based on the minimum detectable phase shift. This change leads us to

$$\mathbf{\Omega}_{min} = \frac{\hbar \Delta\phi_{min}}{2m\boldsymbol{A}}, \tag{1.5}$$

where it is shown that the minimum detectable rotation is inversely proportional to mass. As the mass is increased, the magnitude of $\mathbf{\Omega}_{min}$ gets small therefore increasing sensitivity. Chapter 2 will discuss more on this topic.

The objective of my research is to find methods of improving the reliability of a continuous atom beam interferometer. My work is to increase sensor robustness as it is intended to be used as a navigational gyro. Continuous light use in gyros will allow for smaller, cheaper and more power efficient sensors to be available for shipboard use. It will be a reliable replacement to the RLGNs and a vital tool when the time comes that GPS is no longer available.

1.3.2 Drift

Drift can mean multiple things and it depends on the type of gyroscope in question. Overall, it is related to imperfections in the system. For systems that rely on mechanical stability, imperfections can be found in the gyro bearings and mass imbalances. Other sources could be imperfections in coatings associated with mirrors in the RLGs, for example. RLGNs have been shown to exhibit induced errors as a result of changing temperatures. These errors must be compensated for or extreme position errors can be introduced [7]. Additionally, since the distance traveled is found from acceleration by integrating twice or once for a rotation rate gyro, any small error in acceleration is compounded by showing up in both intergrations. This is known as integration drift. Due to its nature, the atomic sensor is far less susceptible to integration drift.

1.4 Atom Interferometers

Atomic gyroscopes are far less sensitive previously discussed by using the atomic interference to sense the desired rotation rate information. As previously stated, these sensors will have higher sensitivity and smaller size but will have their own limitations to overcome. For our sensor, the continuous atom beam enters a vacuum chamber through a pin size hole to propagate through the laser beam. There is inherent atom beam divergence which causes some atoms not to pass perpendicularly through the light beam and therefore the time of interaction is lengthened. Also, the atoms entering the chamber do not all have the same velocity, so the slower atoms will spend

more time in the laser beam than the faster atoms. These effects lead to longitudinal and transverse averaging and can cause a loss of sensitivity and robustness to system variations. The next chapters will expound on this discussion, and the ways that we are exploring to mitigate these effects.

CHAPTER 2:
Atom Interferometry: Theory

2.1 Introduction

Atom interferometers have been valuable in many fields of research since the early 1990s [8], [9], [10], [11]. They have been useful in confirming many physical constants [12] and have been adapted into the field of accelerometers/gyroscopes [13]. As discussed in the previous chapter, RLGs use light to sense changes in rotation rate. A beam splitter is used to divide a coherent beam of light into two identical beams. Those beams then propagate around a cavity by reflecting off mirrors. In the case of atom interferometers, the roles of atoms and light are reversed. A beam of atoms is developed in a magneto-optical trap (MOT) and propagated through the interferometer. Laser light is precisely controlled to act as either a splitter or mirror. This matter/light interaction can be controlled through light intensity, beam size, light polarization and many other parameters. Through combinations of these parameters, the interaction can cause the atoms to end in a coherent superposition of two states analogous to an optical beam splitter. In a different configuration, the atom's state can switch from one state to another analogous to an optical mirror. As stated in Chapter 1, interferometers work by measuring the relative change in the phase of a particle wave (or matter wave) while traveling between two points over different paths [14]. The phase amplitude for a particle to traverse between two points over a specific path is proportional to the classical trajectory over the same path. An interferometer is sensitive to anything that affects the classical action (e.g., changes in relative path length or any interaction which changes the energy of the particles). Consider a single-atom plane wave described by $|k,i\rangle$, where k is the wave vector and i is the internal state of the atom. The total energy, $E_{total} = \hbar\omega$, of the state is the sum of the internal energy and the kinetic energy. The energy can be simplified to

$$\hbar\omega = E_{int} + \hbar^2 \frac{k^2}{2m}. \tag{2.1}$$

The group velocity is found to be

$$\frac{\partial\omega}{\partial k} = \hbar\frac{k}{m} = v. \tag{2.2}$$

The de Broglie wavelength is given by

$$\lambda_{dB} = \frac{2\pi}{k} = \frac{h}{mv} \approx \frac{4x10^{-7}}{Zv} m, \tag{2.3}$$

where Z is the mass number, and v is the velocity. For cold and ultra-cold atoms, velocities range from millimeters per second to meter per second. Therefore, the de Broglie wavelength may be comparable to 1μm or larger [15]. In addition, since the group velocity is much smaller than that of light waves, the sensitivity of atomic waves to inertial effects is larger. This interaction time allows for rotations and accelerations to create changes to the interfering paths and thus a measurable phase shift. The atom optics, the beam splitters and mirrors that create the multiple path within an interferometer, can be realized in several ways. However, only the laser-induced method will be discussed within this thesis. The coherent oscillation of population from one state to another is referred to as Rabi oscillations. In the case of a single photon transition, this involves excited electronic states that decay too fast to be useful in our application. A Raman process occurs when two lasers act together to produce Rabi oscillations between two ground states. The Raman fields can be either co-propagating or counter-propagating. If the Raman fields are counter-propagating, there is also a momentum transfer [15].

For the entirety of this thesis, Rubidium (Rb) is used as the atom of choice. Rb is used within the gyroscope because of the extensive knowledge on this element and the convenience of cheap, reliable, robust, easy to use lasers coincidentally at the right frequency. Rb is the 37th element and is an alkali metal. This group of metals has been thoroughly researched and show a relatively simple structure with a single valence electron outside the completed shells of the atom. Many inexpensive lasers are available off-the-shelf matching the primary transition wavelength of rubidium 85 (780 nm).

A typical scheme used in these types of atomic interferometers is the $\frac{\pi}{2} - \pi - \frac{\pi}{2}$ sequence of Raman pulses. First, consider a wave packet with mean momentum, p, along the direction of the laser beams and internal state $|1, p\rangle$. The first $\frac{\pi}{2}$ pulse puts the original state $|1, p\rangle$ into a superposition of states $|1, p\rangle$ and $|2, p + 2\hbar k\rangle$. After a period of time, δt, the wave packets will have separated by an amount $\frac{2\hbar k \delta t}{M}$. The π pulse then induces the transitions $|1, p\rangle \rightarrow |2, p + 2\hbar k\rangle$ and $|2, p + 2\hbar k\rangle \rightarrow |1, p\rangle$. After the same time period, δt, the two wave packets merge again with a third pulse ($\pi/2$ again). In the case where the atom beam is set perpendicular to the laser beam, the system can be shown to be the analog to an optical Mach-Zehnder interferometer [9].

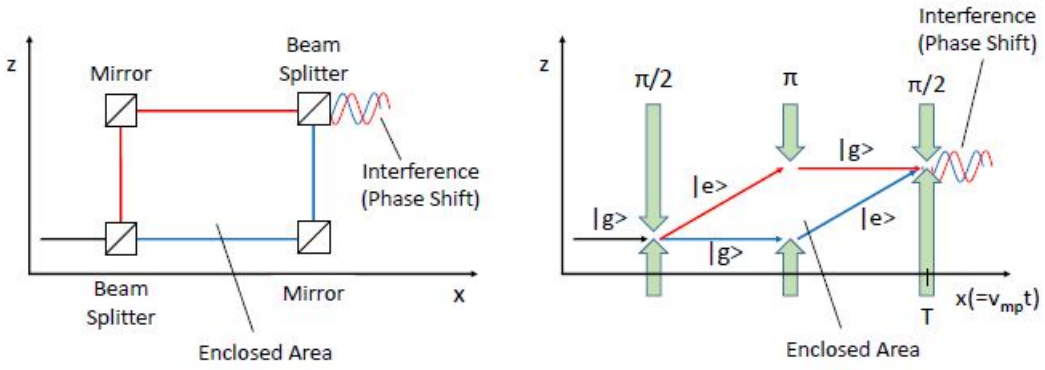

Figure 2.1. Mach-Zehnder interferometer in configurations using light waves (left) and matter waves (right). Matter waves with light pulses are analogous for beam splitter and mirror (left). Note this depicts both a top-down view as well as a representation of state-space. Source [16]

2.2 Current Work

In recent years, tremendous progress in quantum mechanics, atomic manipulation and modern optics has resulted in the winning of the Nobel Prizes for Physics in 1997, 2001, 2005 and 2012. This groundbreaking research had led to direct applications to the atomic interferometers and the ways these sensors perform atomic manipulation. As a result, extremely high sensitivities have been reached with prospects of surpassing those levels. A team in 2001 built an atom interferometer to measure the local acceleration due to gravity, g. Their results claim to have been able to measure g with a resolution of $\frac{\Delta g}{g} = 2x10^{-8}$ in a single 1.3 second measurement cycle [17]. After two days of integration time, the resolution was increased to 10^{-10} [17].

The Atomic Interferometer Gyroscope (AIG) is a continuation of the work done on interferometers. In reality, it is a new technology introduced only within the last couple decades. If designed correctly, it would demonstrate a very high level of sensitivity to rotation resulting in high precision gyroscope. It could ultimately replace the current operational sensors and become the standard gyroscope of the future [4].

2.3 Atomic Interferometer Gyroscope

Atoms are prepared to extremely low temperatures without the need for cryogenics by cooling lasers within an apparatus called a two-dimensional magneto-optical trap (2D-MOT). For this thesis, a

2D MOT is used to cool atoms transversely yet allow atom propagation in one direction. A beam of atoms passes through a pinhole entering a vacuum chamber where the light/matter interactions take place (much more on this later). The prepared atoms are split at the start both in state and physical space. Following a series of further interactions, they are merged at the end point to form a closed loop. There will be a phase shift at the end point in the presence of rotation or acceleration. The fundamental principle of AIG is much like that of the optical gyroscope. The phase shift of an AIG due to rotation is given by [18]

$$\delta\phi_{atom} = \frac{4\pi m}{h}\mathbf{\Omega}\boldsymbol{A} \tag{2.4}$$

The phase shift of optical gyroscope due to rotation is

$$\delta\phi_{light} = \frac{4\pi}{\lambda c}\mathbf{\Omega}\boldsymbol{A}, \tag{2.5}$$

where,
m is the mass of the atom,
h is the plank constant,
$\mathbf{\Omega}$ is the rotation rate vector,
$\boldsymbol{A}$ is the closed loop area vector,
λ is the wavelength of light,
and c is the speed of light.
To compare the sensitivity between an AIG and an optical gyroscope, a ratio of the two equations is taken as

$$\frac{\delta\phi_{atom}}{\delta\phi_{light}} = \frac{m}{\frac{h}{\lambda c}} > 10^{10}. \tag{2.6}$$

So, an AIG in principle is more sensitive than an optical gyroscope to rotation by a factor of 10^{10} [18] since the mass of the atom is much larger than the relative mass of photon, $\frac{h}{\lambda c}$ [3].

2.3.1 Cooling

This research focuses on a small subset of atom interferometer methods namely interferometry using continuous laser beams. The atom source is comprised of transversely cold and longitudinally cool atoms placed in a well-defined initial state via an optical pumping scheme. Our atomic gyroscope uses laser-cooled atoms as the source of the atomic beam used in the interferometer. The sensor requires a continuous supply of cold atoms. Throughout this thesis, the term magneto-optical trap

(MOT) refers to the cold atom beam and region where they are developed. MOTs have been proven to be excellent ways of trapping atoms by meticulously controlling the polarization and frequency of lasers. In a MOT, atoms are cooled to temperatures of a few hundred μK by repeatedly removing energy through atom-photon interactions. A 2D-MOT is a method of trapping atoms in two dimensions while leaving the third dimension free. The result is a collimated beam of cold atoms able to travel in one controlled direction simplifying the physics of any further interactions. The beam is sent through an aperture to the science chamber. Many fields of study have been opened based on the ability to slow atoms specifically research in atomic, molecular, and optical physics (AMO).

To describe this phenomenon more, let us consider a ping-pong ball incident on a bowling ball. With only one ping-pong ball, the bowling ball sees no real effect. Now imagine millions of ping-pong balls analogous to the many photons in a laser beam. They will most definitely affect the bowling ball by imparting momentum through many millions of kicks of very small individual momentum. Bohr's theory explains the action of an atom absorbing an incident photon as long as the photon has the correct frequency. The atom is promoted to an excited state following which it will emit energy in the form of a photon. The act of atomic cooling is to tune the laser to just below that required frequency. We call this red tuned since the incident frequency is slightly less than the atomic transition frequency. The energy absorbed by the atom is less than the energy emitted. The cumulative effect of this interaction over many cycles is a net loss of energy causing the atom to lose kinetic energy in the form of motion and thus lose temperature.

The cooling laser slows the atoms by pushing them in the direction opposite of their velocity. However, the atoms are not affected once the atom's velocity is near zero and are therefore not localized by the cooling lasers. The trapping part of the MOT is performed by permanent magnets. Permanent magnets are arranged in an anti-Helmholtz configuration around the atom chamber and exert a force proportional to their position. As the atoms move away from the center of the trap, the magnets cause the light beams to exert a spatially dependent force in the form of a Zeeman shift in the magnetically sensitive sub levels of the atom [19]. They are ultimately confined to the center of the trap. Our configuration is confined in two dimensions; therefore, atoms are allowed to propagate through a pinhole at the edge of the trap into the experimental vacuum chamber. This description of laser cooling was described using a simplified two-level atom model. In reality, rubidium 85 is much more complex, as shown in Figure 2.2. Most relevant is that the level structure of Rb is such that another laser, referred to as the repump laser, is required. The roll of this laser is described in the next section.

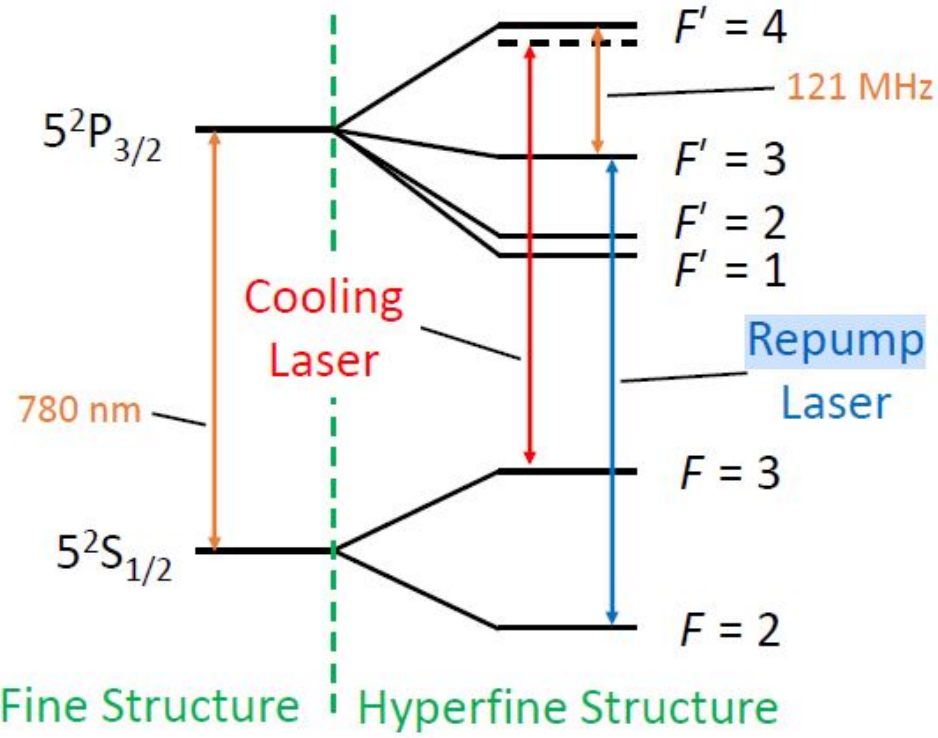

Figure 2.2. The D2 transition of Rubidium 85 (not to scale). The fine level nomenclature comes from the nuclear magnetic resonance (NMR) community ($N^{2S+1}L_J$).

2.3.2 Repump

The cooling laser in our experiment is tuned to the $F = 3$ to $F' = 4$ transition, however, there is a finite probability of off-resonant excitation to $F' = 3$ instead. Selection rules prohibit spontaneous decay from the $F' = 4$ to $F = 2$, while a spontaneous decay from $F' = 3$ to $F = 2$ is allowed. Here, a problem arises since an atom in the $F' = 3$ state has a 50/50 chance of ending in the $F = 2$ state and is lost to the experiment. In the $F = 2$ state, the atoms will no longer be cooled as the cooling laser is now too far from that transition frequency. An answer to this problem is to add a repump laser tuned to the $F' = 3$ to $F = 2$ transition so each time an atom ends up in the $F = 2$ state, the repump laser pushes it back to $F' = 3$ where it has another 50/50 chance to decay to the desire state of $F = 3$. No atoms are lost in this scheme and the temperature of the atoms in the atomic beam is maintained [16].

2.4 Detection

Each time an atom decays to the ground state it emits energy in the form of a photon. Our experiment is designed to measure the number of atoms emitting these photons. Another laser, named the detection laser, along with a photomultiplier tube (PMT) is used for this process. The ground states of interest to us are the $F = 2$ and $F = 3$ state, but the $F = 2$ state is difficult to measure experimentally. For this reason the detection laser is tuned to the $F' = 4$ to $F = 3$. When atoms in the $F = 3$ state pass through the detection laser they will be excited to $F' = 4$ and subsequently decay back to $F = 3$ (minus the few atoms that decay to the $F = 2$). The photons emitted during this process are measured while the atoms that are not in the $F = 3$ pass by without detection. Our experiment is interested in how many atoms end in the $F = 3$ after interactions that occur before the detection process. The atoms exiting the 2-D MOT are in an unknown, incoherent mixture of the states $F = 2$ and $F = 3$. We require that the interferometry experiment start with all the atoms in a well defined state. Because our detection laser is tuned to the $F = 3$ to $F' = 4$ transition, we need all the atoms to start in the $F = 2$ state. We employ another laser to place the atoms in the $F = 2$ state as they enter the vacuum chamber. This process is referred to as optical pumping [16].

2.5 Optical Pumping

To make measurements, we need the atoms to enter the chamber in the $F = 2$ state versus $F = 3$. We cannot use the same cooling light since it imparts a momentum kick that will displace the atom beam away from the pinhole [16]. Instead, an optical pump laser tuned to the $F = 3$ to $F' = 2$ is used. Branching ratios of the D2 transition show that there is a four times greater probability of atoms decaying into the $F = 2$ state from $F' = 2$ vice $F' = 3$. Hence, we use the $F' = 2$ state so far fewer cycles are required for our desired results. The fewer cycles results in a much smaller momentum kick, and the atoms are able to make it through the pinhole.

2.6 Raman and Ramsey

The Raman process involves an atom starting in one ground state and ending in another ground state through coherent two photon transition. In this thesis, the term "Raman process" refers to a stimulated Raman process as we use laser fields to force the transition between states. To drive an atom from one ground state to another prevents the spontaneous emission that would result from being placed in an excited state. Since interferometry is a coherent process, spontaneous emission (an incoherent process) provides nothing useful to our experiment, so we base everything around

the Raman process. To illustrate further, let us use a simple three-level atom arranged in the lambda configuration [20], named after the overall shape of the diagram.

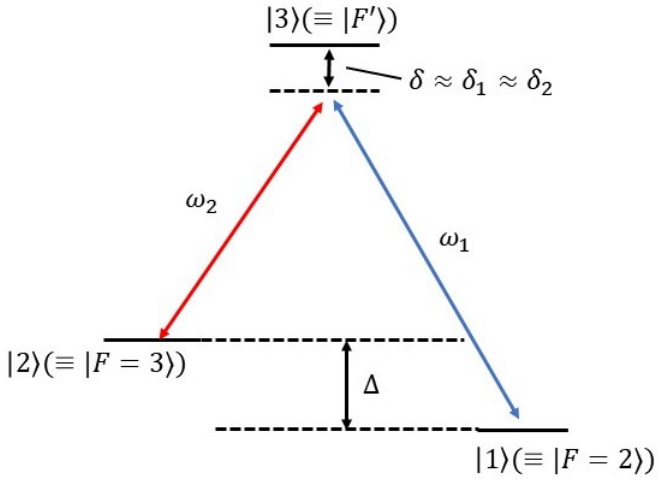

Figure 2.3. Three-level atom with two hyperfine ground states and one excited state. Depicted in the lambda configuration.

Here, the atom has two ground states (labeled $|1\rangle$ and $|2\rangle$) and one excited state ($|3\rangle$). There are now two atomic transitions, which are each driven by a separate laser field. One laser has a frequency, ω_1, close to the $|1\rangle \rightarrow |3\rangle$ transition while the other has frequency, ω_2, close to the $|2\rangle \rightarrow |3\rangle$ transition. Each laser can be detuned such that $\delta_1 = \omega_1 - \omega_{13}$ and $\delta_2 = \omega_2 - \omega_{23}$. There is also a frequency difference between the two ground states referred to as the hyperfine transition frequency or ground state frequency splitting, which results from the hyperfine interaction. It is denoted by Δ. It is large enough to allow each laser to couple to only its respective transition. To drive a Raman process, the laser detunings are chosen so $\delta_1 - \delta_2 - \Delta \approx 0$, which means the system is near two-photon resonance. In this configuration, the excited sate can be adiabatically eliminated to form a two-level system. With the excited state now a virtual state, the two ground states become the new ground and excited state of the two-level model with no spontaneous decay.

Ramsey interference is an intermediate step toward an atom interferometer. It was developed by Norman Ramsey earning him a Nobel prize [21], [11]. It is the simplest form of atomic interference as it utilizes only a $\pi/2 - \pi/2$ sequence of pulses with no momentum kick. The mathematics of Ramsey interference is identical to the mathematics of the famous Young's double slit interference.

The two optical pulses play the role of the two slits. Today, it is used in atomic clocks and has applications in many fields of scientific study. Two pairs of light beams are used to create interference patterns that provide useful information on atom wave properties. Each of the pairs of light beams are arranged to act as beam splitters to create superposition of two atomic ground states. This results in a series of fringes contained in an envelope. It can be used as a diagnostic tool in determining the effectiveness of the $\pi/2$ pulses as well as characterizing the effects of velocity averaging.

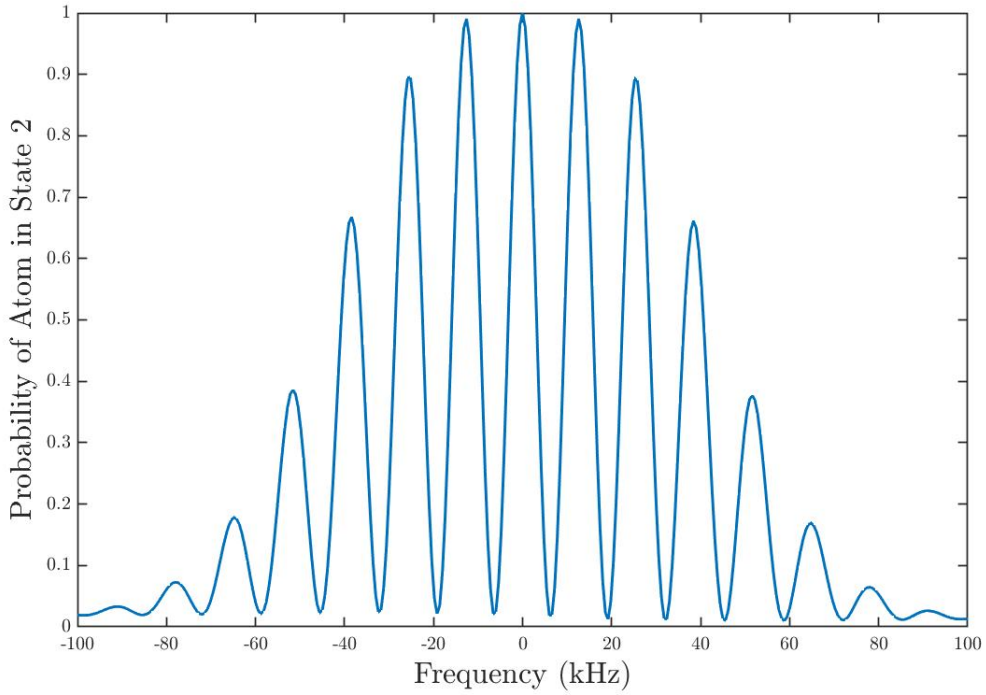

Figure 2.4. Ramsey spectrum with one atom velocity. The interference pattern is a result of constructive and deconstructive interference as the atom passes through two consecutive $\pi/2$ pulses.

2.7 Velocity Averaging

The interaction time between atom and laser directly affects the atoms resultant state. Ultimately, this time will dictate whether the atom will see a π or $\pi/2$ pulse or something in between. To

explain these terms further, the π pulse refers to the complete transition of state,

$$|g\rangle \rightarrow i\,|e\rangle\,, \tag{2.7}$$
$$|e\rangle \rightarrow i\,|g\rangle\,, \tag{2.8}$$

from ground to excited state or vice versa analogous to a mirror in optics. Similarly, the $\pi/2$ pulse causes a coherent superposition of the two states,

$$|g\rangle \rightarrow \frac{1}{\sqrt{2}}(|g\rangle + i\,|e\rangle), \tag{2.9}$$
$$|e\rangle \rightarrow \frac{i}{\sqrt{2}}(|g\rangle - i\,|e\rangle). \tag{2.10}$$

This interaction is then analogous to a beam splitter. These terms both come down to time of interaction where the π pulse is on for twice the time as the $\pi/2$ pulse. A pulse in this context is the interaction time between the atom and laser as the atom propagates through the chamber. Faster atoms will have shorter pulses while slower atoms will take longer to get past through the laser field. If the atom beam was somehow able to produce single velocity atoms, it would be possible to design a configuration with the desired pulse length to achieve the intended goal by simply choosing a laser beam diameter so that the atomic transit time corresponds to the time of a $\pi/2$ pulse. However, in our experiment the atoms enter the chamber with a spread of velocities given by a Maxwell Boltzmann distribution with most probable velocity of ≈7 m/s which has been previously measured using our sensor [5]. This velocity spread causes a spread in pulse times and has a large effect on the results. In our modeling (see Chapter 4), the atomic velocity distribution is described by

$$P(v) = \frac{2v^3}{v_{mp}^4} e^{\frac{-v^2}{v_{mp}^2}}, \tag{2.11}$$

where

$$v_{mp} = \sqrt{\frac{2k_B T}{m}}. \tag{2.12}$$

Here, T is the temperature, m the atomic mass, and k_B is the Boltzmann constant. The effect of the velocity averaging is the loss of fringe structure (see Figure 2.5) to the Raman and Ramsey

spectrum. The curve is the results of a Ramsey interference like in Figure 2.4 but the pulse times are given by $\frac{d}{v}$ and then averaged over the velocity distribution. Ω is chosen such that

$$\Omega\frac{d}{v} = \frac{\pi}{2}.$$

The specific goal of my thesis is to apply a stimulated Raman adiabatic passage (STIRAP) pulse sequence (discussed in the next chapter) to see if there is a less negative effect due to the velocity spread.

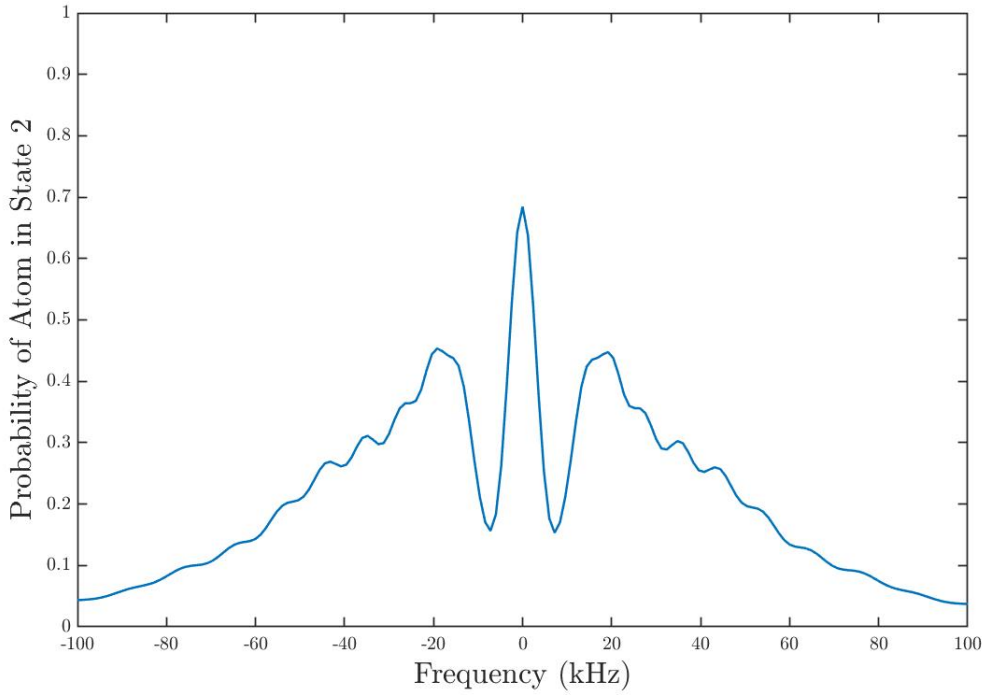

Figure 2.5. Ramsey spectrum with velocity averaging. The interference pattern is a result of constructive and deconstructive interference as the atom passes through two consecutive $\pi/2$ pulses. However, here the atom velocity can be any value up to ≈30 m/s. Note the loss of fringe structure.

2.8 Stimulated Raman Adiabatic Passage

Stimulated Raman adiabatic passage (STIRAP)has been studied extensively over the past 25 years and has a steady foothold in the community of atomic, molecular, and optical physics [22]. It was

first fully presented in 1990 by a team working on techniques for atomic population transfer [23]. STIRAP is a method of coupling two quantum states of an atom with two radiation fields through a virtual state. Because the dynamics involve a virtual state instead of a real state, it is immune to the deleterious effects of spontaneous emission, and therefore STIRAP has its advantages in controlled population transfer when compared to other methods. The acronym STIRAP was first introduced because the first studies of the method were done in the lambda, Λ, linkage, which resembles a typical Raman process. It does not exhibit the same losses to spontaneous emission from an intermediate state as traditional Raman processes, even though coupling lasts much longer than the radiative lifetime. Second, and most importantly, it is more robust [24] to experimental imperfections, such as atom velocity, laser intensity, and pulse shape [25]. We intend to implement STIRAP arranged laser beams in an atomic gyroscope to decrease the interferometer's sensitivity to velocity averaging and thereby increase the sensors efficiency when compared to a conventional Raman arrangement.

2.9 Basics

All analyses for this thesis are based on the three-level lambda system as seen in Figure 2.3. Upon initial inspection, it would appear that spontaneous emission from state 3 would be detrimental to the control of population transfer since the radiative decay could occur to a state other than the desired final state. Of course, this would greatly lower the system's overall efficiency. Also, spontaneous emission, even into the correct state, is uncontrolled and incoherent. The remarkable feature of STIRAP is it does not actually populate the intermediate state as the atom population transfers from one state to another. Since there is no population of the intermediate state, there is no corresponding spontaneous decay [22]. STIRAP allows for the complete coherent population transfer of an atom from one quantum state to another. Two coherent, radiation fields couple the intermediate state with the two ground states forming what seems like a bridge. The laser linking state 1 ($|1\rangle$ and the intermediate state ($|3\rangle$) is referred to as the P (pump) laser. The laser linking state 2 ($|2\rangle$) and the intermediate state ($|3\rangle$) is referred to as the S (Stokes) laser [25].

In the case of this thesis, the originating ground state will always be state 1 (e.g, we assume we optically pump everything into state 1 before the start of the STIRAP experiment). The atom/light interaction occurs as the atom passes through the laser beams driving the STIRAP process. We can think of this interaction as a pulse of light with a time equal to the laser beam diameter divided by the atom velocity (e.g, the atom's transit time through the laser field). The atom can either travel through two spatially overlapping laser beams, as in the case of traditional Raman spectroscopy, or

sequentially based on their separated spatial orientation as in STIRAP. When the S laser is arranged before the P, the system is deemed counterintuitive since the non-populated state is linked first. Counterintuitive order causes the system dynamics to take place in a so-called dark state. The dark state is a coherent superposition of the initial and target states [26]. There must be an overlap of the two beams for the coherence to be maintained through the transfer.

In the counterintuitive pulse sequence, the Stokes laser couples the two empty states, $|2\rangle$ and $|3\rangle$. Since the two states are empty, there is no population transfer and therefore no change in the population of state $|1\rangle$. However, the Stokes laser has a large impact on the subsequent transfer process. The Stokes laser creates a coherent superposition of the ground states $|2\rangle$ and the excited state $|3\rangle$, which are initially empty. Next, the pump laser couples the populated state $|1\rangle$ with this coherent superposition state and a resultant dark state is formed [22]. A dark state is a state in which the pump laser cannot transfer population to the excited state $|3\rangle$ where radiative decay is expected. The population is instead directly transferred into state $|2\rangle$ eliminating the excited state and effectively negating any losses due to decay.

THIS PAGE INTENTIONALLY LEFT BLANK

CHAPTER 3:
Modeling: The Schrödinger Approach

3.1 Introduction

Modeling is necessary to validate our hypothesis as well as to see the effects of varying parameters within the system and help guide experiments. Initial modeling is done via the Schrödinger approach because the resulting two-level approximation is often sufficient for analysis. Because the two-level approach avoids rapidly oscillating terms, the numerical simulations run orders of magnitude faster than the equations from the density matrix approach. However, the density matrix method was ultimately adopted as we were required to properly include spontaneous emission, to more accurately simulate the experiment. As stated earlier, spontaneous emission is minimized by use of STIRAP, but it is not completely removed. The density matrix model allows us to account for this effect.

3.2 The Schrödinger Theory

A three-level atom can be modeled using the Schrödinger approach starting with the semi-classical Hamiltonian

$$\mathcal{H} = \hbar\Delta \left|2\right\rangle \left\langle 2\right| + \hbar\omega_{13} \left|3\right\rangle \left\langle 3\right| - \hat{\boldsymbol{\mu}} \cdot \boldsymbol{E}, \tag{3.1a}$$

where

$$\hat{\boldsymbol{\mu}} = \boldsymbol{\mu}_{23} \left|2\right\rangle \left\langle 3\right| + \boldsymbol{\mu}_{13} \left|1\right\rangle \left\langle 3\right| + \boldsymbol{\mu}_{23}^{*} \left|3\right\rangle \left\langle 2\right| + \boldsymbol{\mu}_{13}^{*} \left|3\right\rangle \left\langle 1\right|, \tag{3.1b}$$

and

$$\boldsymbol{E} = \mathcal{E}_1 \boldsymbol{\epsilon}_1 e^{i(\omega_1 t - k_1 z)} + \mathcal{E}_2 \boldsymbol{\epsilon}_2 e^{i(\omega_2 t - k_2 z)}. \tag{3.1c}$$

In the above equations, $\hat{\mu}$ represents the atomic dipole moment and $\boldsymbol{E}$ is the electric field. The total laser field consists of two modes of amplitude $\mathcal{E}_i$, frequencies ω_i, wave number k_i, and polarization vector $\boldsymbol{\epsilon}_i$ ($i = 1, 2$). The Hamiltonian obeys the time-dependent Schrodinger equation,

$$i\hbar \frac{\partial \psi}{\partial t} = H\psi. \tag{3.2}$$

The state of the atom at anytime, t, can be written in terms of the bare atomic basis states as

$$|\psi(t)\rangle = c_1(t)\,|1\rangle + c_2(t)\,|2\rangle + c_3(t)\,|3\rangle\,. \tag{3.3}$$

The resulting equations for the time varying amplitudes, $c_i(t)$, are found to be

$$\dot{\tilde{c}_1} = \frac{i}{2}\Omega_1^*\tilde{c_3}, \tag{3.4a}$$

$$\dot{\tilde{c}_2} = -i[(\delta_2 - \delta_1) - (k_2 - k_1)v]\tilde{c_2} + \frac{i}{2}\Omega_2^*\tilde{c_3}, \tag{3.4b}$$

$$\dot{\tilde{c}_3} = i(\delta_1 - k_1 v)\tilde{c_3} + \frac{i}{2}\Omega_2\tilde{c_2} + \frac{i}{2}\Omega_1\tilde{c_1}, \tag{3.4c}$$

where the tilde over the state amplitudes indicates the amplitude in the rotating basis (see Equation A.12a). Here, δ_1 and δ_2 represent the single photon detunings of each laser from its respective transition, and Ω_1 and Ω_2 represent the single photon Rabi frequencies.

An approximation is used to assist in finding an analytic solution to the equations of motion (or at least equations amenable to easy numerical solutions). A more complete derivation can be found in the Appendix. The Hamiltonian will contain terms oscillating at a frequency $(\omega_{Laser} - \omega_{Atom})$ and $(\omega_{Laser} + \omega_{Atom})$. The rotating wave approximation (RWA) assumes the frequencies close to the atomic resonance are the dominant ones. As a result, terms within the Hamiltonian which oscillate very rapidly are removed. This approximation has been shown to be valid when close to resonance and when the relative intensity of the laser is low. The former is also known as detuning and in terms of magnitude, is much less than the summation of the frequencies [27]. Therefore, the oscillatory terms of the Hamiltonian that contain the summation will essentially average to zero over any applicable time scale. For this reason, the terms can be neglected. One can think of the system as evolving is a frame rotation at the laser frequency, and the counter rotating terms are the ones that average away. Below, we sketch the numerical integration of the final set of equations of motion, but the full derivation can be found in Section A.1 of the Appendix.

If we rewrite Equation 3.3 as a column vector in the rotating basis, then

$$\psi = \begin{bmatrix} \tilde{c_1} \\ \tilde{c_2} \\ \tilde{c_3} \end{bmatrix}. \tag{3.5}$$

The right side of Equation 3.4a can be written as $L\psi$, where

$$L = \begin{bmatrix} 0 * \tilde{c_1} & 0 * \tilde{c_2} & \frac{i}{2}\Omega_1^* \tilde{c_3} \\ 0 * \tilde{c_1} & -i(\delta_2 - \delta_1)\tilde{c_2} & \frac{i}{2}\Omega_2^* \tilde{c_3} \\ \frac{i}{2}\Omega_1 \tilde{c_1} & \frac{i}{2}\Omega_2 \tilde{c_2} & i\delta_1 \tilde{c_3} \end{bmatrix}, \tag{3.6}$$

so that Equation 3.4a becomes

$$\frac{d\psi}{dt} = L\psi. \tag{3.7}$$

Equation 3.7 is a simple vector-matrix equation, which as discussed in the next section, is easily solved numerically.

3.3 Adiabatic Following

A defining property of STIRAP is the alignment of the atomic state vector with the dark state. To maintain the alignment, there must be slow variations in the mixing angle. The mixing angle is defined by

$$tan(\theta(t)) = \frac{\Omega_1}{\Omega_2}. \tag{3.8}$$

The condition for adiabatic evolution during STIRAP was derived by Kuklinski [28] as

$$\Omega_{rms}(t) \gg \mid \dot{\theta}(t) \mid = \frac{\mid \Omega_2(t)\dot{\Omega}_1(t) - \Omega_1(t)\dot{\Omega}_2(t) \mid}{\Omega_1(t)^2 + \Omega_2(t)^2}, \tag{3.9}$$

where $\Omega_1(t)$ and $\Omega_2(t)$ are the Rabi frequencies for states 1 and 2, respectively. When the lasers have a smooth shape, a global abiabaticity criterion can be shown when the time average of $\dot{\theta}$ is taken to be

$$< \dot{\theta}_{av} >= \frac{\pi}{2}\Delta\tau, \tag{3.10}$$

where $\Delta\tau$ is the interaction time. This should not exceed the Ω_{rms}. The numerical simulation efforts of other research groups [28], found that

$$\Omega_{rms}(t)\Delta\tau >> 1. \tag{3.11}$$

Additionally, the pulse area is proportional to the peak Rabi frequency, Ω_0, and the interaction time. It follows that there is now a minimum pulse area,

$$A_{min} < \Omega_{max}\Delta t, \tag{3.12}$$

to achieve the desired adiabatic population transfer. We see from Equation 3.12 that for a given interaction time, the Rabi frequency can be increased to meet the required limit, which is a useful characteristic of the system. The adiabatic condition described allows for overall robustness against variations of system parameters such as atom velocity. Due to the relatively long interaction time of our atom/light interaction and the variable peak Rabi frequency, our system meets the requirements to exhibit adiabatic characteristics.

3.4 MATLAB

Equation 3.7 can be solved numerically using a standard numerical solver. Here, we used the MATLAB numerical solver ODE45. Due to the inherent high frequencies within the system; on the order of 3 GHz, the frequency terms are normalized by a factor, $\beta = 2\pi(3MHz)$, as this is the natural decay rate of the atom. This scaling will save computational space and time. In order to try to match the conditions of the experiment and learn more from the system dynamics, we

- set the single photon Rabi frequencies to a constant, $\Omega_1 = \Omega_2 = 10\beta$.
- set the single photon detuning, δ_1, and δ_2, to 50β.
- set the initial population to be 100% in the 1^{st} state (e.g., $\tilde{c}_1(0) = 1$, $\tilde{c}_2(0) = \tilde{c}_3(0) = 0$).

Figure 3.1 shows the results of integrating Equation 3.7 with the parameters specified above. We find that, largely, the population simply oscillates coherently between two ground states with nearly zero population in the excited state. It is precisely because of these coherent oscillations that Raman transitions are used in atom interferometry.

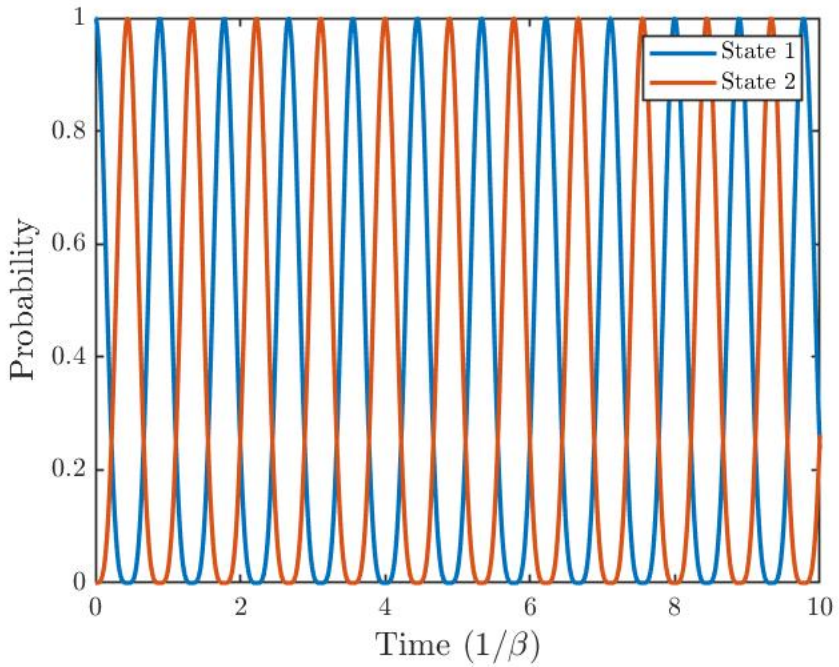

Figure 3.1. Population transfer between two ground states. The population oscillates between the two states at a high frequency due to the system being on resonance. Here, $\Omega_1 = \Omega_2 = 10\beta$ and $\delta_1 = \delta_2 = 0\beta$.

Furthermore, other challenges operating near single photon resonance occur. Even though the system demonstrates coherence, we are not in the adiabatic regime. For this, we need to be off resonance where the single photon detuning, $\delta_1 = \delta_2 > 50\beta$. This is consistent with the adiabatic approximation that the Raman Rabi frequency, Ω_R, is given by [29]

$$\Omega_R = \frac{\Omega_1 \Omega_2}{2\delta} \tag{3.13}$$

in the large single photon limit, where $\delta = \delta_1 = \delta_2$. The frequency of oscillation slows dramatically, as seen in Figure 3.2. We see the difference between the oscillation in these two cases is a factor of 2 as expected.

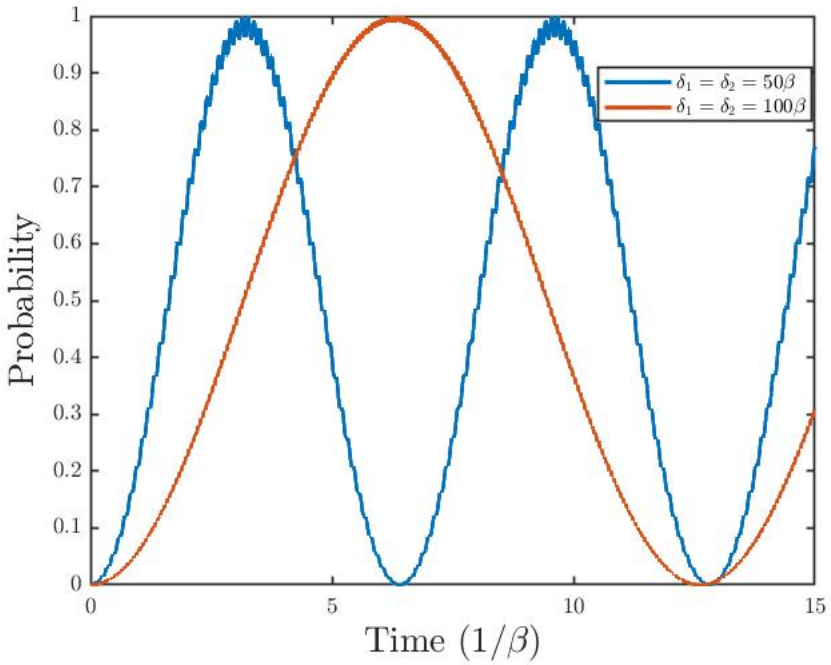

Figure 3.2. Population transfer between two ground states. The population oscillates between the two states over time. Here, $\Omega_1 = \Omega_2 = 10\beta$ and $\delta_1 = \delta_2 = 50\beta$.

The model accurately simulates a stationary atom irradiated by a laser pulse of constant intensity for a fixed period of time (e.g., a square pulse). However, the experiment involves atoms from an atomic beam traveling through a laser beam of Gaussian profile. In the atom's frame of reference, it is irradiated by a laser pulse where intensity varies as a Gaussian in time with a temporal width determined by the Gaussian spatial width of the laser beam divided by the velocity of the atom.

To better match the experiment, the code previously described was adapted so that the single photon Rabi frequency, $\Omega_i (i = 1, 2)$ now becomes a function of time. The laser beam in the simulations is taken to be 2 mm in diameter. As discussed earlier, a typical atom velocity has been found in earlier experiments [16] to be $\approx$7 m/s resulting in the pulse duration of 285 μsec as shown in the Figure 3.3. Here, the two laser beams corresponding to the two different transitions, namely the pump and Stokes field, are assumed to be completely overlapping in space. Under these conditions, the equations simulate the traditional Raman process [16], but with a Gaussian temporal shape.

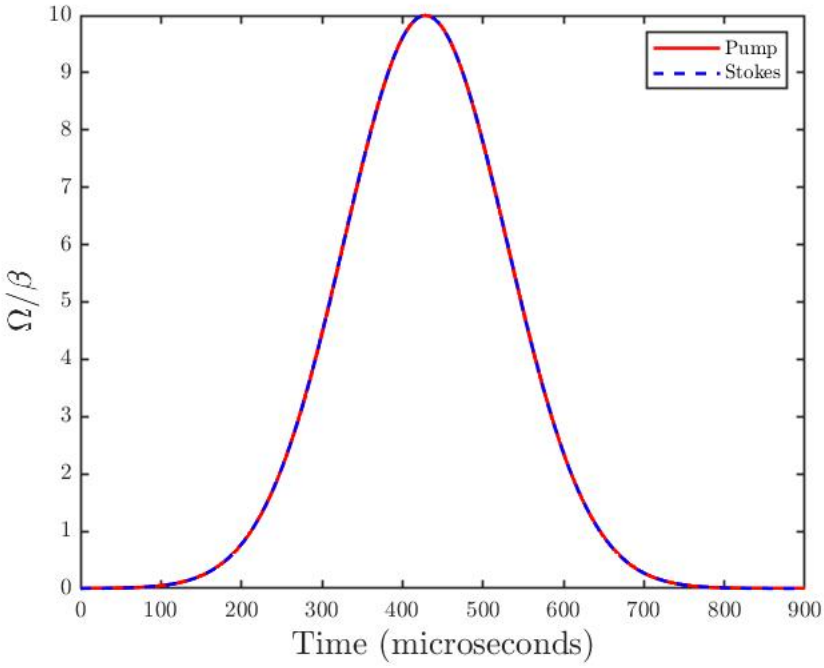

Figure 3.3. A gaussian pulse representing the atom/light interaction. The pump and Stokes beams are both present here with complete spatial overlap. Here, peak Rabi frequency $(\Omega_0)_1 = (\Omega_0)_2 = 10\beta$.

Equation 3.7 is is now integrated using the time varying electric field depicted in 3.3. This is a better representation to the actual atom/light interaction. The peak Rabi frequency, $(\Omega_0)_1 = (\Omega_0)_2 = 10\beta$, while $\delta_1 = \delta_2 = 100\beta$.

Figure 3.4 shows the rapid oscillations of the population in state 2 through the entirety of the interaction. The "chirp" on the oscillation frequency is due to the Gaussian nature of the pulse intensity. It is precisely this pulse-width dependence that causes loss of contrast in the interferometer. While the oscillations in population do die away and the population reaches a stable steady state when the laser pulses are over, the final value of the population is strongly dependent of the pulse width of the laser as experienced by the atom, which unavoidably varies due to the velocity spread of the atoms in the atomic beam.

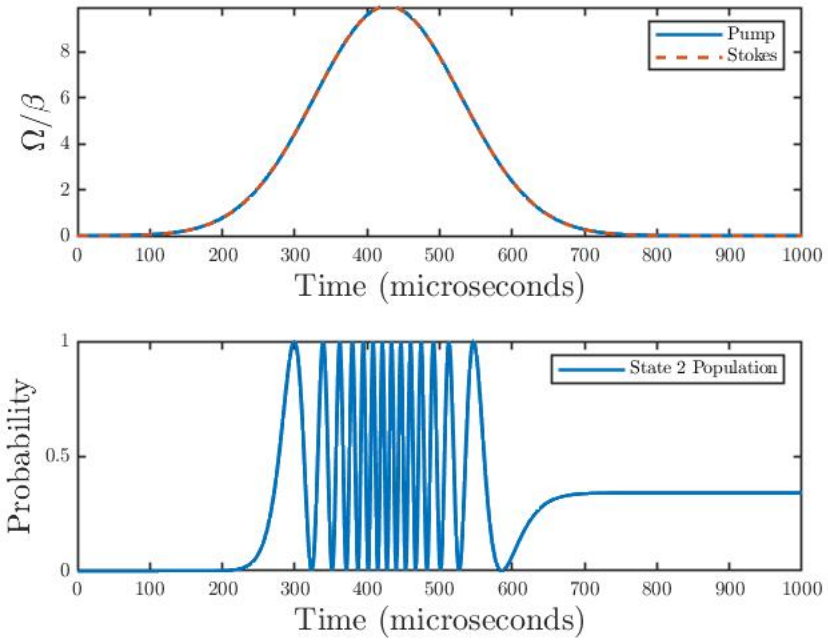

Figure 3.4. Population transfer for state 2 over time with a time varying intensity. Here, $(\Omega_0)_1 = (\Omega_0)_2 = 10\beta$ and $\delta_1 = \delta_2 = 100\beta$

The next step is to adjust the spatial overlap of the two beams and arrange them in such a way as to have the laser corresponding to the $|2\rangle \rightarrow |3\rangle$ transition be incident first followed by the laser coupling the $|1\rangle \rightarrow |3\rangle$ transition. In the code, this corresponds to the two pulses being temporally displaced. In the actual experiment the lasers are physically displaced, and the atom's velocity converts the spatial separation of beams into a temporal displacement of pulses. This arrangement results in the counterintuitive STIRAP configuration. The laser beams are separated by the optimal spacing of 1.5 mm center to center as determined by other research [22] and verified by our own simulations (shown later in Chapter 4). The numerical results of such an arrangement are depicted in Figure 3.5.

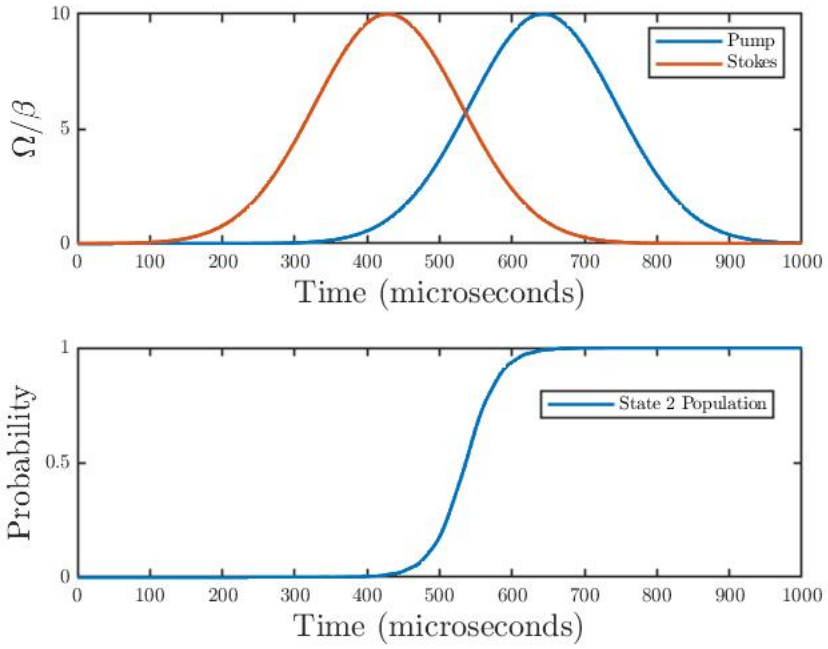

Figure 3.5. Population transfer for state 2 over time with a time varying intensity. Here, $(\Omega_0)_1 = (\Omega_0)_2 = 10\beta$ and $\delta_1 = \delta_2 = 100\beta$. Note the absence of oscillations during the atom/light interaction.

A much more controlled transition from the initial state $|1\rangle$ to the final state $|2\rangle$ is apparent in this figure as the population of state $|2\rangle$ reaches 100% after the interaction. It is apparent here that as long as the atom interacts for at least $\approx$ 600 microseconds, the atom's quantum state will be changed by 100% with little sensitivity to the pulse duration. This result is very powerful and is the reason STIRAP has become so popular with current research in multiple disciplines. To improve the overall model, we transitioned our simulations to the density matrix model. Specifically, we have found that, in order to achieve good signal-to-noise ratio (SNR) in our system, we need to work somewhere close to resonance (e.g., $\delta_1 = \delta_2 = 50\beta$), which makes the approximations $\delta >> \beta$ somewhat questionable. If this assumption is violated, spontaneous emission can no longer be ignored. We address this by switching to a density matrix formulation, which accounts for spontaneous emission. A more realistic model, with fewer assumptions, can now be made, but at the expense of a more complicated code that is much more computationally intensive.

THIS PAGE INTENTIONALLY LEFT BLANK

CHAPTER 4:
Modeling: Density Matrix Approach

4.1 Density Matrix Theory

In this section, a three-level atom model is investigated using the density matrix approach, which permits spontaneous decay to be included in the calculations. The Hamiltonian used for this model is the same as before (Equation 3.1a). It is given as

$$\mathcal{H} = \hbar\Delta \left|2\right\rangle \left\langle 2\right| + \hbar\omega_{13} \left|3\right\rangle \left\langle 3\right| - \hat{\boldsymbol{\mu}} \cdot \boldsymbol{E},$$

where (see Equation 3.1b)

$$\hat{\boldsymbol{\mu}} = \boldsymbol{\mu}_{23} \left|2\right\rangle \left\langle 3\right| + \boldsymbol{\mu}_{13} \left|1\right\rangle \left\langle 3\right| + \boldsymbol{\mu}_{23}^{*} \left|3\right\rangle \left\langle 2\right| + \boldsymbol{\mu}_{13}^{*} \left|3\right\rangle \left\langle 1\right|, \tag{4.1}$$

and

$$\boldsymbol{E} = \mathcal{E}_1 \boldsymbol{\epsilon}_1 e^{i(\omega_1 t - k_1 z)} + \mathcal{E}_2 \boldsymbol{\epsilon}_2 e^{i(\omega_2 t - k_2 z)}. \tag{4.2}$$

In writing Equation 4.1, it is implicitly assumed that there is no optical transition between states $|1\rangle$ and $|2\rangle$ which is a condition well satisfied in our experiments due to atomic selection rules. All other symbols (e.g., ϵ_i, k_i, ω_i) have the same meaning as before. The Schrödinger equation describes how states evolve in time while the Von Neuman equation describes how the density operator evolves in time. Thus, we begin with the Von Neuman equation of motion for the density operator,

$$\dot{\rho} = -\frac{i}{\hbar} \left[\mathcal{H}, \rho\right].$$

The full density matrix derivation can be found in Section A.2 of the Appendix. We end up with the eight coupled differential equations

$$
\begin{aligned}
\dot{\psi}_1 &= -\{\gamma_{12} - i\left[(\delta_2 - \delta_1) - (k_2 - k_1)\, v\right]\}\, \psi_1 + \frac{i}{2}\left[\Omega_1^* \psi_7 - \Omega_2 \psi_2\right] \\
\dot{\psi}_2 &= -\left[\gamma_{13} + i\,(\delta_1 - k_1 v)\right] \psi_2 + \frac{i}{2}\left[\Omega_1^*\,(2\psi_8 + \psi_4 - 1) - \Omega_2^* \psi_1\right] \\
\dot{\psi}_3 &= -\{\gamma_{12} + i\left[(\delta_2 - \delta_1) - (k_2 - k_1)\, v\right]\}\, \psi_3 - \frac{i}{2}\left[\Omega_1 \psi_5 - \Omega_2^* \psi_6\right] \\
\dot{\psi}_4 &= (W_{32} - W_{12})\, \psi_8 - (W_{12} + W_{21})\, \psi_4 + \frac{i}{2}\left(\Omega_2^* \psi_7 - \Omega_2 \psi_5\right) + W_{12} \\
\dot{\psi}_5 &= -\left[\gamma_{23} + i\,(\delta_2 - k_2 v)\right] \psi_5 + \frac{i}{2}\left[\Omega_2^*\,(\psi_8 - \psi_4) - \Omega_1^* \psi_3\right] \\
\dot{\psi}_6 &= -\left[\gamma_{13} - i\,(\delta_1 - k_1 v)\right] \psi_6 - \frac{i}{2}\left[\Omega_1\,(2\psi_8 + \psi_4 - 1) - \Omega_2 \psi_3\right] \\
\dot{\psi}_7 &= -\left[\gamma_{23} - i\,(\delta_2 - k_2 v)\right] \psi_7 - \frac{i}{2}\left[\Omega_2\,(\psi_8 - \psi_4) - \Omega_1 \psi_1\right] \\
\dot{\psi}_8 &= -(W_{31} + W_{32})\, \psi_8 + \frac{i}{2}\left(\Omega_2 \psi_5 + \Omega_1 \psi_2 - \Omega_2^* \psi_7 - \Omega_1^* \psi_6\right),
\end{aligned}
\tag{4.3}
$$

where the elements of ψ are density matrix components written as

$$
\psi = \begin{bmatrix} \tilde{\rho}_{12} & \tilde{\rho}_{13} & \tilde{\rho}_{21} & \tilde{\rho}_{22} & \tilde{\rho}_{23} & \tilde{\rho}_{31} & \tilde{\rho}_{32} & \tilde{\rho}_{33} \end{bmatrix}^T .
$$

W_{ij} is defined as the incoherent transition rate from state i to state j. For optical transitions, even at room temperature, $W_{ij} = 0$ for $i < j$ (i.e., upward transitions). Therefore, $W_{13} = W_{23} = 0$. However, this is not true for microwave transitions, so we have to leave W_{13} and W_{23} in the equations for generality. These decay rates are usually very small, so for the simulations, we take $W_{12} = W_{21} = 0$. Additionally, γ_{ij} is the decay rate of the off-diagonal elements of the density matrix. In free space, this is given by [30]

$$
\gamma_{ij} = \frac{1}{2} \sum_k (W_{ij} + W_{jk}). \tag{4.4}
$$

These 8 equations can be written in a compact form as

$$
\dot{\psi} = L\psi + I,
$$

where the 8x8 matrix, L, and the column vector, I, follow from Equation 4.11. One cannot simply integrate and write

$$\begin{aligned} \frac{d\psi}{L\psi + I} &= dt, \\ \psi(t) &= L^{-1}(e^{Lt}[L\psi(0) + I] - I). \end{aligned}$$

This is because it only works [31] when

$$[L(t), \int_0^t L(t)dt] = 0,$$

which in our case is unfortunately not true. Therefore, we turned to numerical ODE solvers to obtain solutions.

As with the Schrödinger picture, the two light beams are taken to be 2 mm wide. For the purpose of this simulation, we simulate a mono-energetic atomic beam with atomic velocity of 7 m/s. As before, a time varying intensity is modeled using a Gaussian pulse with a maximum intensity in the center of the beam set by Ω_0. Initially, the beams were set to completely overlap. The entire atom population is assumed to be initially in state 1, which is consistent with the experiment. In this section, the population of state 2 is only plotted since we saw from the previous section what very little population ends up in state 3. Since population is conserved, the total population in state 1 and state 2 must add to 1. The single photon detuning is adjusted to see how the transfer of state is affected.

We began our investigations by considering the case of being on single and two photon resonance. Figure 4.1 shows the rapid development of the coherent superposition of the 2 ground states. This resultant behavior works well for a $\pi/2$ pulse (beam splitter). However, as previously discussed, an interferometer works on the $\pi/2 - \pi - \pi/2$ beam configuration also known as spin echo. We have investigated the model further on resonance by changing system parameters and have found there is no arrangement to achieve the needed π pulse (i.e., 100% population transfer into state 2). Since the Raman light all originates from one laser source, there is no way in our current configuration to separaetly detune individual pairs of beams. As guided by traditional Raman spectroscopy, we next investigated increasing the single photon detuning to $\delta_1 = \delta_2 = 50\beta$.

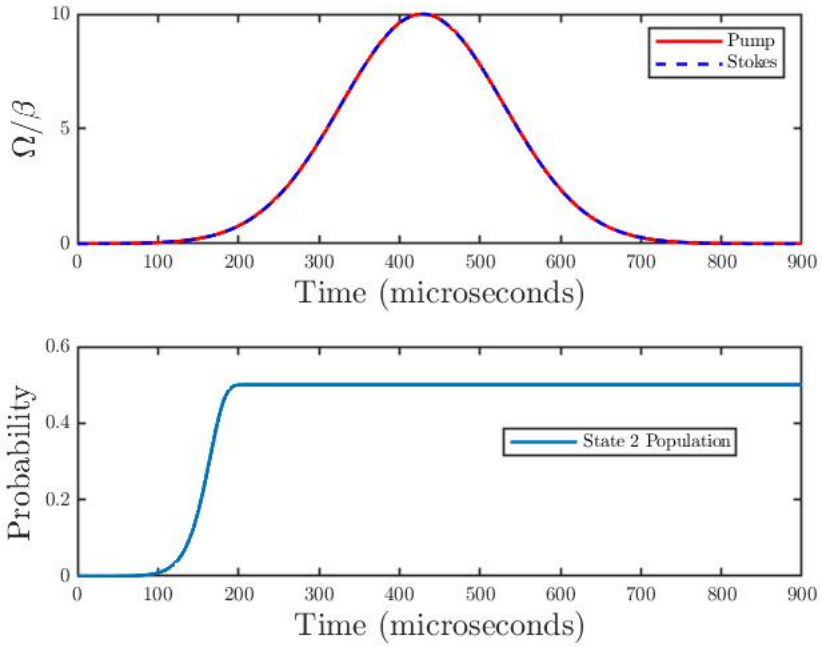

Figure 4.1. Population transfer for state 2 over time with a time varying intensity within the density matrix scheme. Here, $(\Omega_0)_1 = (\Omega_0)_2 = 10\beta$ and $\delta_1 = \delta_2 = 0\beta$. Note the abrupt change to a population of 0.5. This behavior would work for a $\pi/2$ pulse; however, we have found there is no way to reach 100% transfer

Now we see rapid oscillations in the population, reminiscent of the traditional Raman, during the time the pulses are on. The oscillations then damp away leaving half of the population in state 2.

As the single photon detuning is increased, there is no longer the smooth and rapid transfer into the dark state but rather rapid oscillations that damp out to a steady state value. The decay in oscillation amplitude throughout the interaction in Figure 4.2 is a characteristic of spontaneous decay. We expected and verified numerically that the rate of decay of the oscillations would decrease as δ is increased. Although not definitely proven here, the resultant state of the system is an incoherent mixture of ground states as a result of the spontaneous decay. We also have not pursued this arrangement further, since the rapid oscillations would also impact the sensor by introducing timing errors when different atom velocities are introduced, which would defeat the point of using STIRAP. We continued to develop our model to find a more stable behavior.

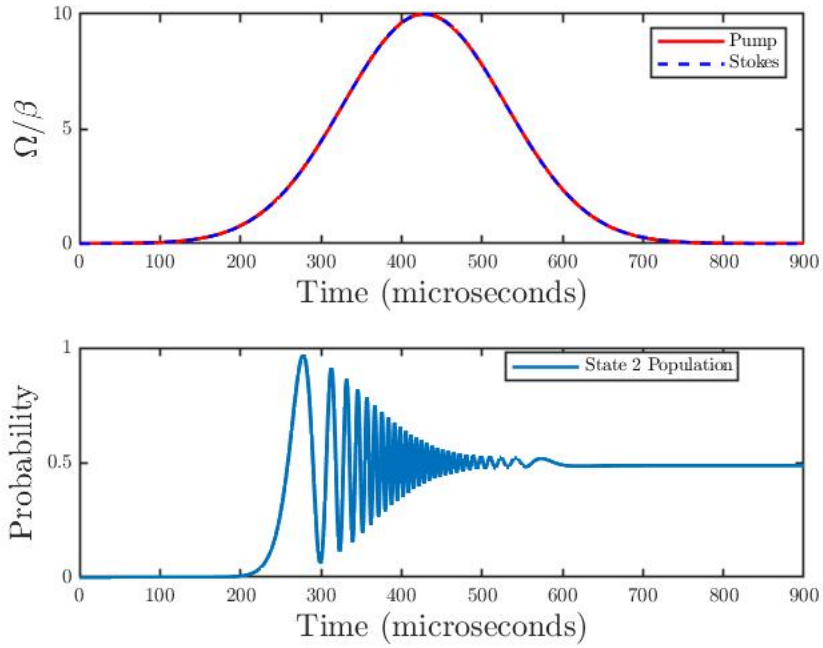

Figure 4.2. Population transfer for state 2 over time with a time varying intensity within the density matrix scheme. Here, $(\Omega_0)_1 = (\Omega_0)_2 = 10\beta$ and $\delta_1 = \delta_2 = 50\beta$. The oscillations like the ones from the Schrödinger picture have returned. However, now spontaneous decay causes as loss of coherence and the oscillations decay away.

Finally, we implement the STIRAP separated beam configuration and find encouraging results. STIRAP involves the overlapping of laser beams to achieve the coherent transfer of atoms from state to state. Zero separation, for example, would be a complete overlap of the two beams. Prior to studying the full implementation of STIRAP in an atom interferometer configuration, we first investigated the effects of varying the amount of pulse overlap on the total population transfer and the efficiency of transfer. The two pulses, namely pump and Stokes, are incrementally shifted from a configuration of the pump pulse occurring prior to the Stokes (the negative region of separation in Figure 4.4) to the Stokes occurring prior to the pump (the positive region of separation in Figure 4.4).

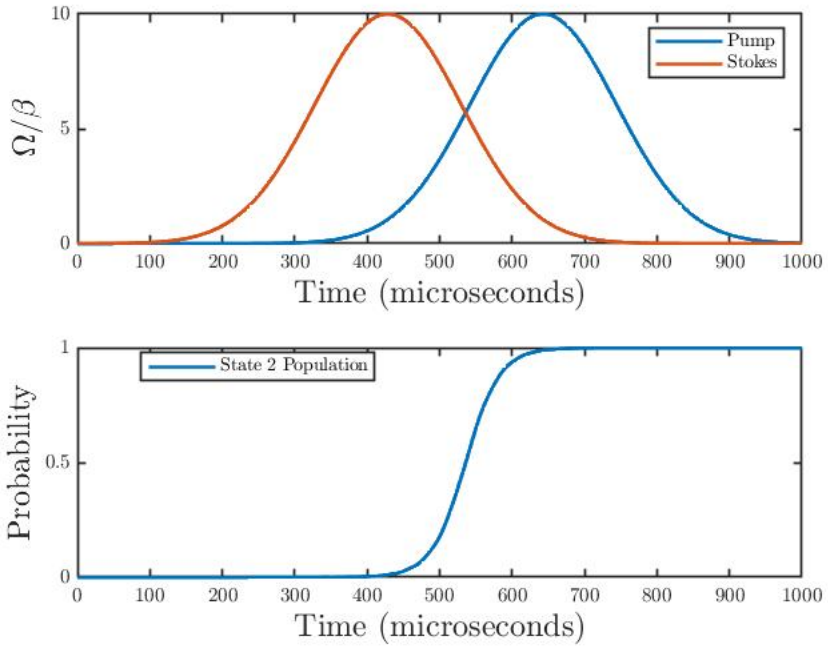

Figure 4.3. Population transfer for state 2 over time with a time varying intensity within the density matrix scheme. The laser beams are overlapped in the counterintuitive STIRAP configuration. Here, $(\Omega_0)_1 = (\Omega_0)_2 = 10\beta$ and $\delta_1 = \delta_2 = 100\beta$ for both beams. Note the controlled transition of state through the atom/light interaction.

STIRAP relies on the partial overlap of the P and S lasers as had been discussed. Bergmann, Theuer, and Shore showed that there is a region of overlap consistent with full population transfer [22]. Outside that region, efficiency is drastically reduced (see Figure 4.4). To experimentally implement STIRAP, it is useful to know the optimal pulse separation. Figure 4.4 gives us the population transfer as a function of beam separation (as measured from beam center to beam center). In these simulations, we took $(\Omega_0)_1 = (\Omega_0)_2 = 10\beta$ for several different values of single photon detuning. As the center of the beams are moved apart, a region of optimal placement can be seen near 1.5 mm. The variation of the population transfer efficiency with the delay of interaction of the two lasers is a characteristic signature of the STIRAP process.

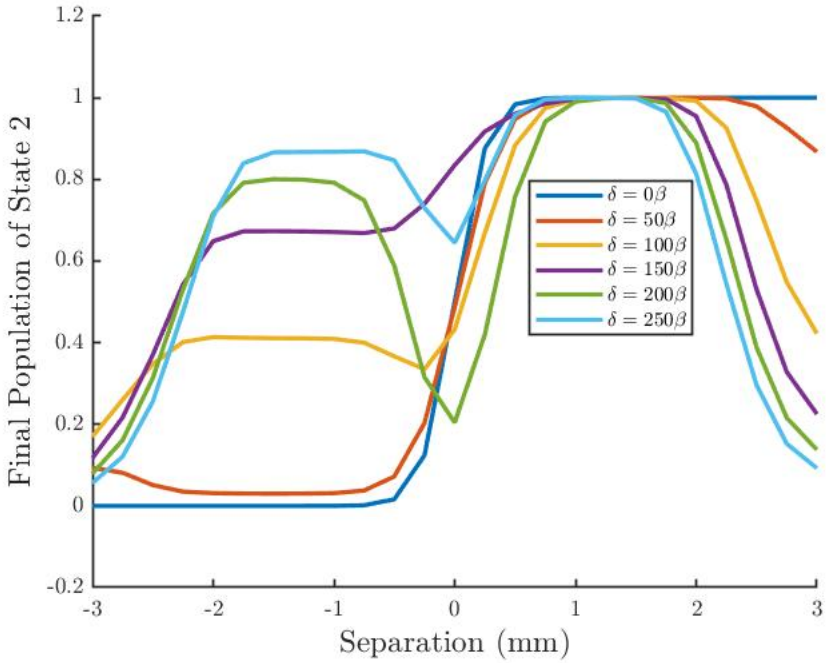

Figure 4.4. Final population of state 2 as a function of beam separation. There is a large dependence on separation near 0 (complete overlap). Once the separation reached 1.5 mm there is complete transfer until the beam are pulled too far apart. Here, $(\Omega_0)_1 = (\Omega_0)_2 = 10\beta$.

In the region where the pump beam interacts first with the atoms (the region of negative separation), the pump field acts as an optical pump since the atoms originate in state 1 which coincides with the pump beam transition. Additionally, there seems to be a large dependence of single photon detuning in that region. Further investigation needs to be made into why the final state 2 population increases as the system is brought farther from resonance. However, this point is moot because as an optical pump, the atoms are moved to the other ground state but in an incoherent manner. This incoherence causes this configuration to be useless for the purposes of an interferometer. This study does conclude that the optimal spatial orientation of the two beams is to have the center of the Stokes beam be 1.5 mm prior to the center of the pump beam, consistent with existing literature [22].

The beam spacing of 1.5 mm is the separation inserted into Figure 4.3 and will be used for all future models unless otherwise stated. To show the power of STIRAP even further, the system was investigated under the same conditions as Figures 4.1 and 4.2 but with two beams offset from each other at the optimal spacing. The prior oscillations and abrupt changes are gone as now there is a smooth, controlled transfer of population from one ground state to another seen in Figure 4.5.

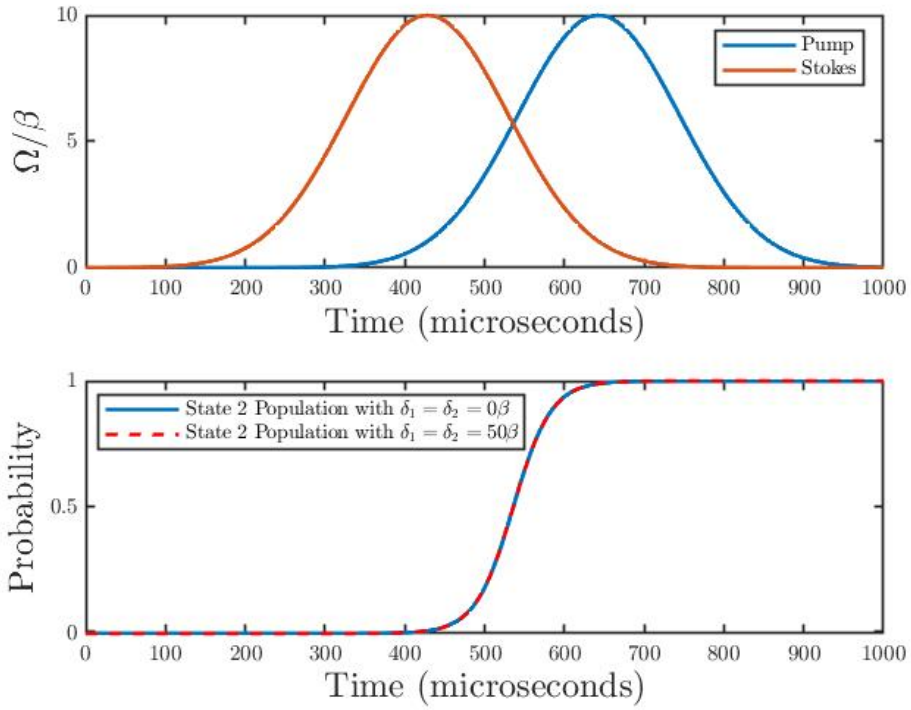

Figure 4.5. Population transfer for state 2 over time with a time varying intensity within the density matrix scheme. The laser beams are overlapped in the counterintuitive STIRAP configuration with separation of 1.5 mm. Here, $(\Omega_0)_1 = (\Omega_0)_2 = 10\beta$, $\delta_1 = \delta_2 = 0\beta$ (blue solid line) and $\delta_1 = \delta_2 = 50\beta$ (red dashed line). Note there is no difference between the two conditions.

The population in Figure 4.5 is observed to transfer completely to state 2 during the matter/light interaction with negligible oscillations even at $\delta_1 = \delta_2 = 0\beta$. An increase in single photon detuning to 50β and 100β as in Figure 4.3 has no effect of the population transfer verifying STIRAP's robustness to changes in system parameters.

The conclusion to this point is that STIRAP can be useful for the generation of a π pulse which is robust to experimental imperfections. However, as mentioned before, atom interferometers use a $\pi/2-\pi-\pi/2$ protocol. The next step in our modeling is to determine system parameters that result in an even coherent superposition of the two ground states (the $\pi/2$ pulse). With two consecutive $\pi/2$ pulses, known as a Ramsey sequence, an interference pattern can be made for system analysis and optimization. There are two main approaches which will be covered here. First, the laser intensity in lowered until half of the population can be transferred, as shown in Figure 4.6. There is a plateau at 50% which is desired for its robustness to pulse errors. However, the final value is sensitive to

the laser power.

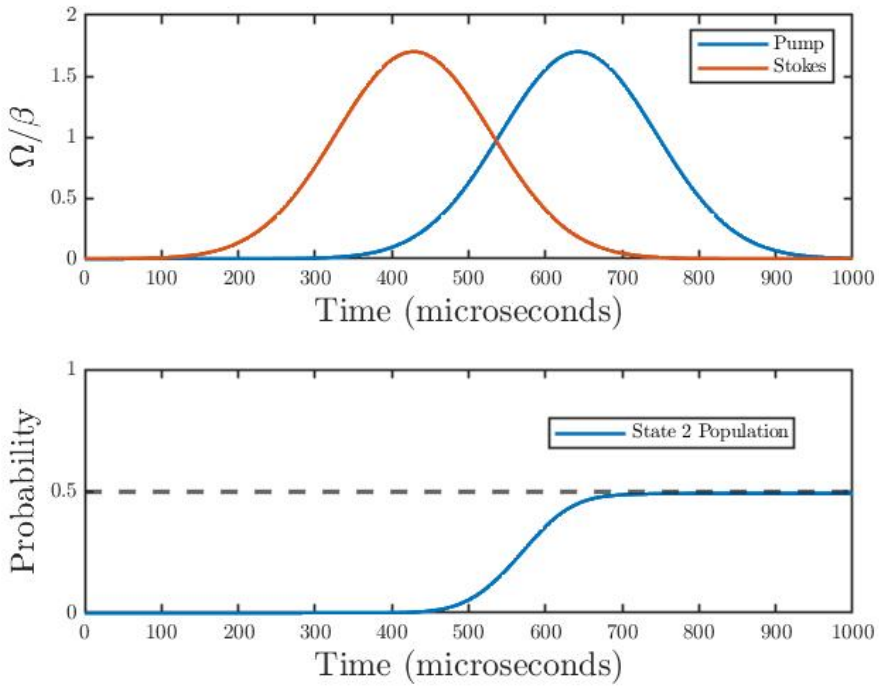

Figure 4.6. Population transfer for state 2 over time with a time varying, spatially separated intensity. The population of state 2 builds from zero to 50 percent as desired in a pi/2 pulse. Here, $(\Omega_0)_1 = (\Omega_0)_2 = 1.7\beta$ and $\delta_1 = \delta_2 = 50\beta$.

Figure 4.7 shows a relationship between the laser intensity and the final population percentage of state 2 for three cases of single photon detuning. As expected, the population transfer reaches 100 percent and maintains as intensity is raised. Within these typical levels of detuning, there is no advantage of raising maximum intensity past $\Omega \approx (5-6)\beta$. Power is simply wasted past that point.

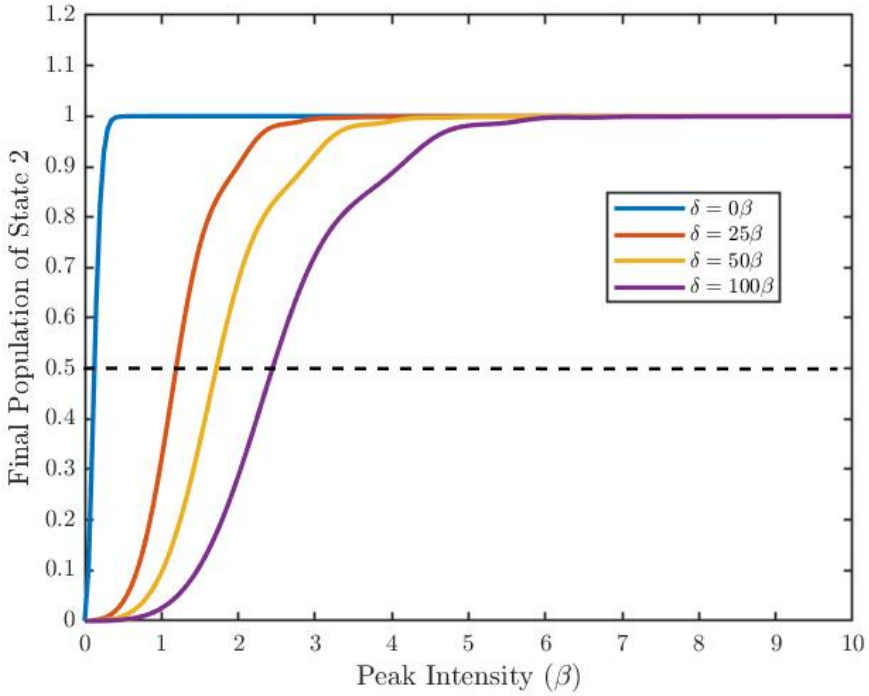

Figure 4.7. Final population value of state 2 as a function of intensity for three cases of single photon detuning. The laser intensity does not have to be raised past $(\Omega_0)_1 = (\Omega_0)_2 = 4\beta - 6\beta$ for these typical levels of detuning.

Figure 4.7 shows the corresponding value of intensity to reach 50% population is approximately 1.7β in the case of the medium detuning of $\delta_1 = \delta_2 = 50\beta$. It is clear from the steepness of the curves in Figure 4.7 that changes in intensity lessen the overall robustness when compared to the full STIRAP. However, the benefit of having a π or $\pi/2$ pulse outweighs the negative of decreased robustness in this case. The value of 1.7β was taken into the STIRAP model in Figure 4.6 to see a population transfer from the original state 1 to an equal superposition of state 1 and state 2. Another method of achieving controlled population transfer as suggested in the literature [24] is by adjusting the beam diameters with respect to each other. The total area under the pulses in indicative of the amount of energy transferred to the atom from each laser field. As the overlap area increases, the resulting population transfer efficiency to state 2 will be higher.

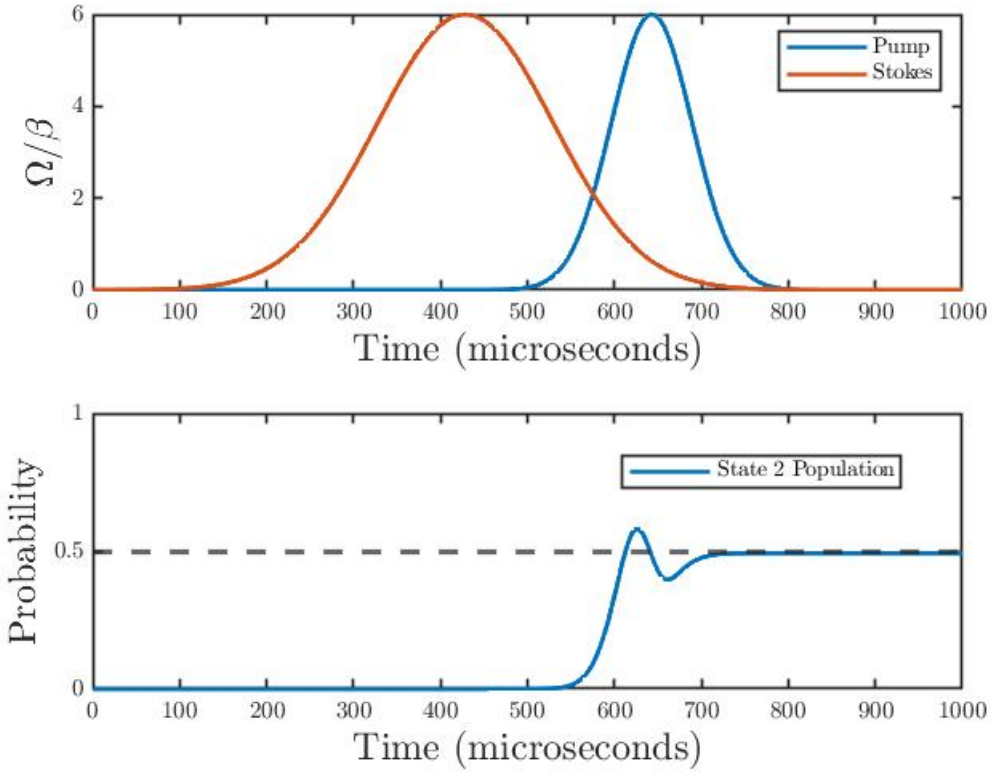

Figure 4.8. Population transfer of 50% to state 2 with a laser configuration where the pump beam has a diameter approximately half the size of the Stokes. Here, $(\Omega_0)_1 = (\Omega_0)_2 = 6\beta$ and $\delta_1 = \delta_2 = 100\beta$.

Therefore, to lower the transfer to the desired 50%, the area must be reduced. This can be done by narrowing one of the beams, as depicted in Figure 4.8. However, we found there is far more variation in state 2 population in this case when compared to that of intensity variation. Figure 4.9 shows the relationship between the width of the pump beam and the final state of the atom for the case of maximum Rabi frequency $(\Omega_0)_1 = (\Omega_0)_2 = 6\beta$. The stronger dependence on beam size is likely due to the fact that the dynamics depend linearly on power but inversely quadratic on beam size. For this reason, all future beam splitters will be modeled using a reduction in intensity.

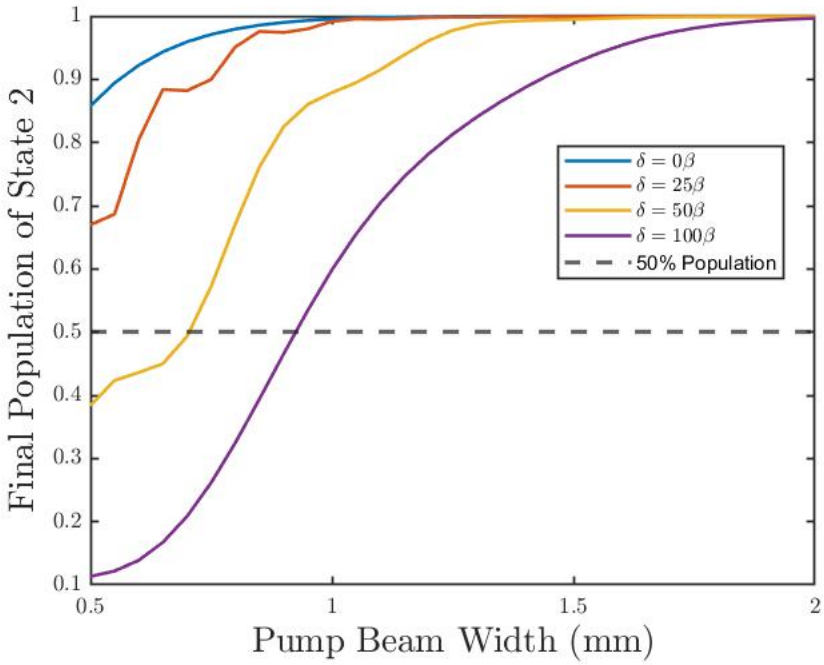

Figure 4.9. Final population of state 2 as a function of pump beam diameter. There is more variation in population in these three cases compared to Figure 4.7. Here, $(\Omega_0)_1 = (\Omega_0)_2 = 6\beta$.

Now that one $\pi/2$ pulse can be modeled, it is easy to duplicate a second one in attempts to generate a Ramsey interference pattern.

4.2 Adding a Second Set of Pulses

In this section, we discuss the results of the simulation when a second set of pulses are added to the model (the so-called Ramsey sequence). For the model, the same parameters are used in building the second set of pulses with the only difference being the time the second set of pulses are applied with respect to the first pair of pulses. For initial analysis, the parameters used to create π pulses were used. The maximum Rabi frequency was set to $(\Omega_0)_1 = (\Omega_0)_2 = 5\beta$ and single photon detuning to $\delta_1 = \delta_2 = 50\beta$. A complete overlap of the beams is simulated below as a reference.

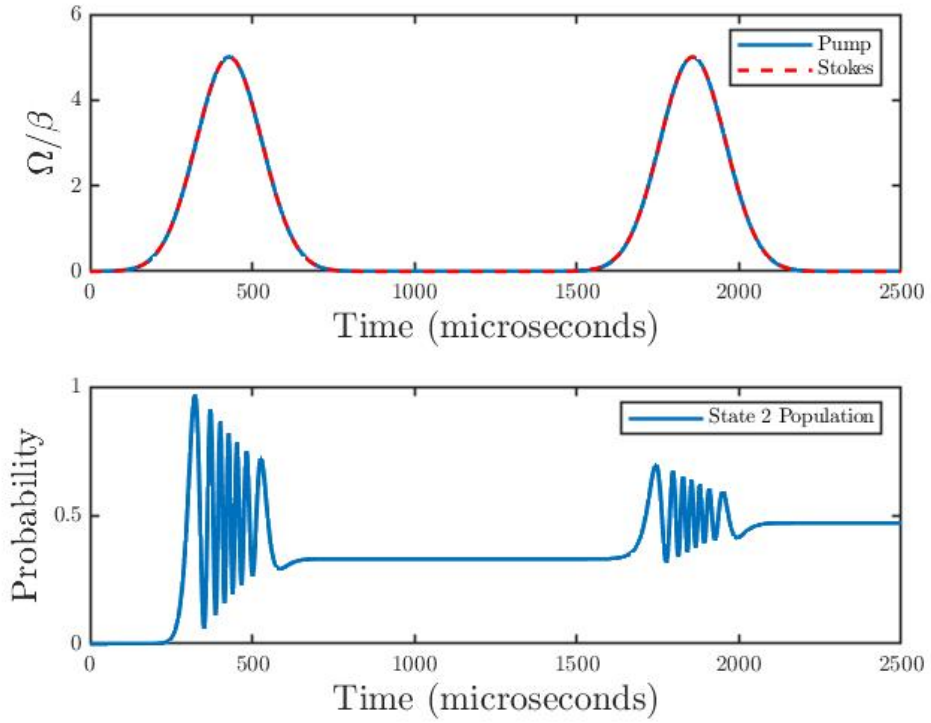

Figure 4.10. The time varying population of state 2 as a result of two consecutive sets of P and S beams. The beams are completely overlapped with $(\Omega_0)_1 = (\Omega_0)_2 = 5\beta$ and $\delta_1 = \delta_2 = 50\beta$.

A similar behavior is noticed in the population of state 2 compared to a single pulse interaction (see Figure 4.2). Rapid oscillations are a result of the system being close to resonance. There is also a loss of coherence due to the spontaneous decay. These negative effects are profound since the provided intensity is expected to cause a complete population transfer.

We now compare to STIRAP as the beams of each pulse are physically separated to a peak-to-peak distance of 1.5 mm. The other properties are kept the same.

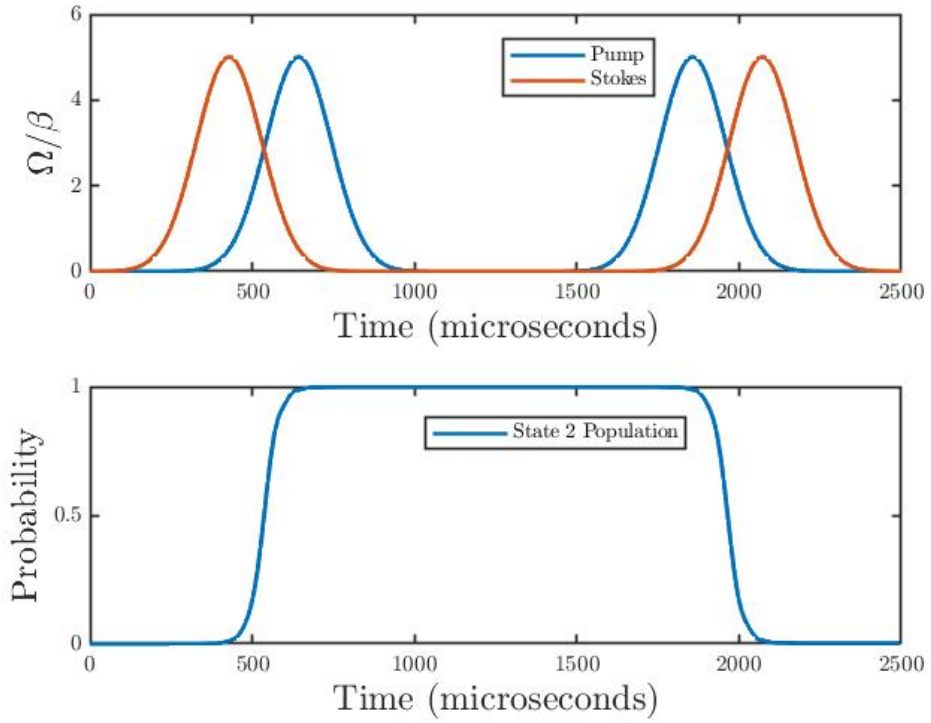

Figure 4.11. The time varying population of state 2 as a result of two consecutive encounters with partially overlapping P and S lasers. Note the absence of oscillations, and the complete population transfers in both encounters. Here, $(\Omega_0)_1 = (\Omega_0)_2 = 5\beta$ and $\delta_1 = \delta_2 = 50\beta$.

Figure 4.11 is indicative of expected behavior for an atom interaction with the two pulse configuration. The first set of P and S lasers causes a complete population transfer from state 1 to state 2. The second set has the opposite arrangement with the P laser interacting before the S laser. This arrangement causes a complete transfer back to state 1. The laser beams are acting as an atomic version of optical mirrors. Now, by reducing the intensity to one where a 50% of the atoms reach the excited state and setting the second set of pulses to a similar P before S configuration, we have two sequential $\pi/2$ pulses or a Ramsey scheme. However, the order of Stokes and pump now matters with STIRAP. Figure 4.12 depicts the population transfer over the two sets of $\pi/2$ pulses, where the red dashed line corresponds to the (Stokes-pump)-(Stokes-pump) arrangement and the blue line corresponds to the (Stokes-pump)-(pump-Stokes) arrangement.

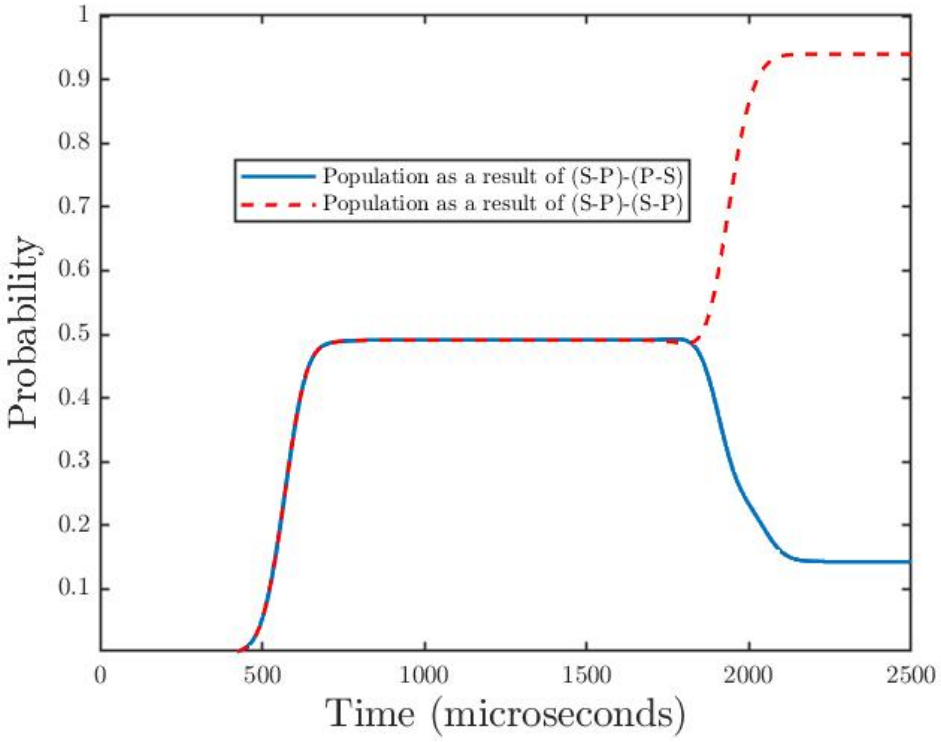

Figure 4.12. A comparison of the time varying population of state 2 as a result of two consecutive encounters with partially overlapping P and S lasers configured as $\pi/2$ pulses. The blue line represents the laser orientation of (S-P)-(P-S). The dashed red line represents the laser orientation of (S-P)-(S-P). Here, $(\Omega_0)_1 = (\Omega_0)_2 = 5\beta$ and $\delta_1 = \delta_2 = 50\beta$.

Notice how the state 2 population will be maximized in one configuration while minimized in the other. We choose to use the version depicted by the red line since the detection system of our sensor is designed to detect atoms from state 2, which correspnds to the (S-P)-(S-P) configuration.

With the desired parameters for two sequential $\pi/2$ pulses, we are able to generate a Ramsey interference pattern within the density matrix model. This interference pattern is generated by varying the two photon detuning, $\delta_2 - \delta_1$, over a range of several kHz. In all the previous analysis $\delta_1 = \delta_2$, therefore forcing two photon detuning to be 0. Within these small variations, the system witnesses either coherent constructive or coherent deconstructive interference and as a result creates fringes within the Raman envelope. The following two plots were generated from my code and compare the case of complete beam overlap and STIRAP. They both incorporate velocity averaging, as discussed in Section 2.7.

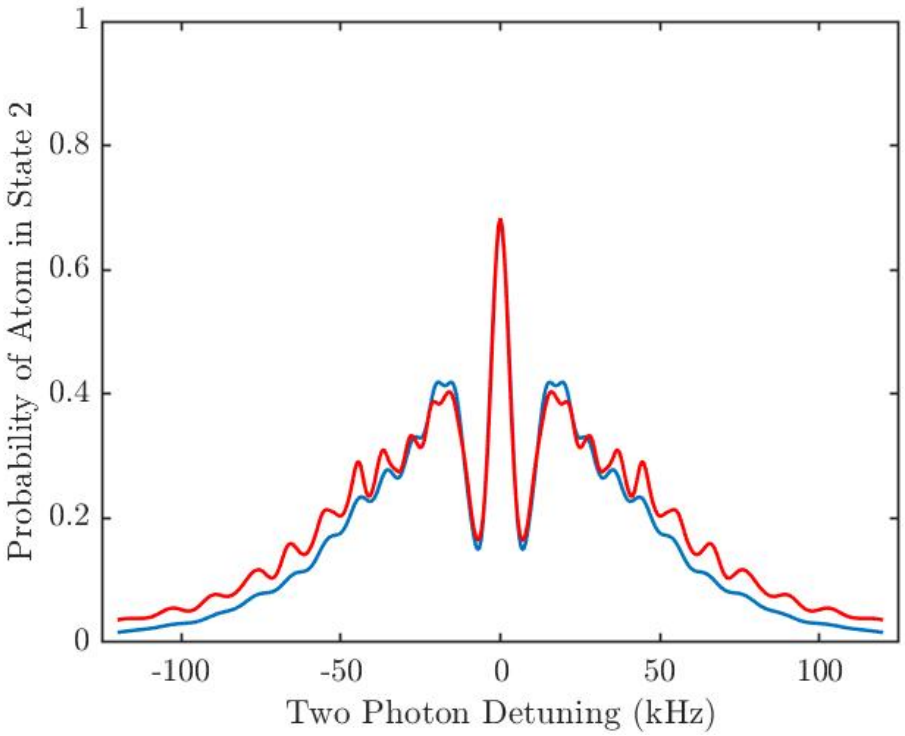

Figure 4.13. Velocity averaged Ramsey spectrum where S and P completely overlap (blue line) and in the STIRAP arrangement (red line).

Notice in both plots that the magnitudes of the spectrum are essentially the same meaning there is no loss in efficiency from one method to the other. However, the STIRAP spectrum shows more pronounced fringing indicative of a higher level of coherence. It is expected that further optimization of the STIRAP conditions will result in better contrast. Better coherence is alone enough to continue with the implementation if STIRAP into our dual beam atomic gyroscope. The next chapter describes the experimental setup of the sensor and how we intend to implement STIRAP as a method of atom excitation.

CHAPTER 5:
Atom Interferometry: Experiment

5.1 Introduction

Our experiment consists of a vacuum chamber in which on one side a 2D-MOT is generated and through it an atom beam propagates to the opposite side of the vacuum chamber to the detection laser. A series of Raman beams enter in the middle to cause the desired quantum shifts. The entire sensor is mounted on top of a rotating platform for future analysis in a frame rotating with a known rotation rate.

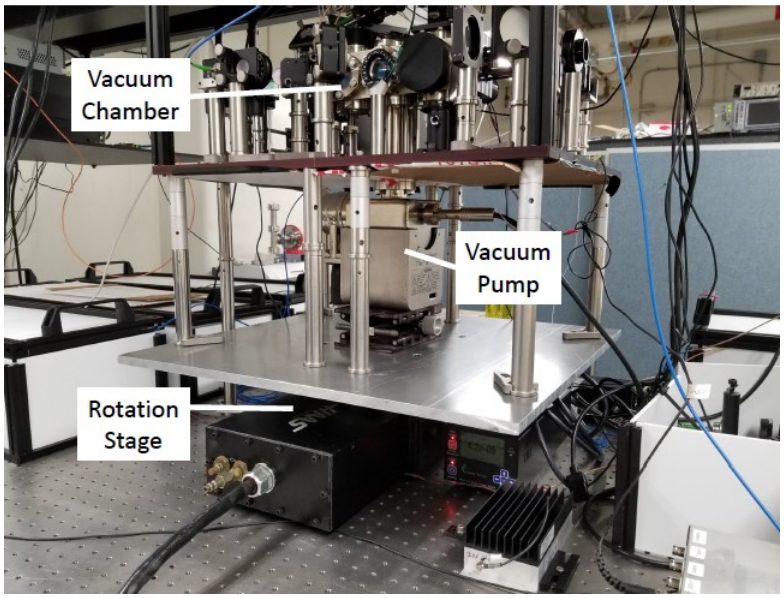

Figure 5.1. The apparatus on top of the rotation stage.

The 2D-MOT is created on one side of the chamber with the cooling, repump, and optical pump laser beams. Light from two distributed feedback lasers (Eagleyard EYP-DFB-0780-00080-1500-TOC03), named cooling and repump, is combined and separated into 2 orthogonal, retroreflected beams which become incident on the chamber. The chamber is filled with gaseous rubidium atoms in their natural state. The combined light traps the atoms in 2 dimensions leaving atoms free to enter the vacuum chamber as a cold beam. The vacuum chamber is approximately 9 inches long

and made of stainless steel. It features a series of three 2.75 in ConFlat^{TM} flange sight windows on each side. The atom beam travels through a pinhole sized aperture and into the main body of the vacuum chamber. The beam is then subjected to various light interactions through those sight windows. After the beam of atoms interact with the Raman lasers, a detection laser (Eagleyard EYP-DFB-0780-00080-1500-TOC03 distributed feedback laser) tuned to the $F = 3$ to $F' = 4$ transition is used to create excite the atoms. The subsequent scattering of photons is measured on a photomultiplier tube (PMT) (Hamamatsu H6780-20) aligned in the third window. The detection laser is also used to optimize the MOT during its formation as it can measure the fluorescence from atoms in the beam when no interaction is present. A full description of the various lasers and methods of building the current sensor can be found in [16]. My project is to change the method of generating and applying the Raman beams into the chamber at the middle window.

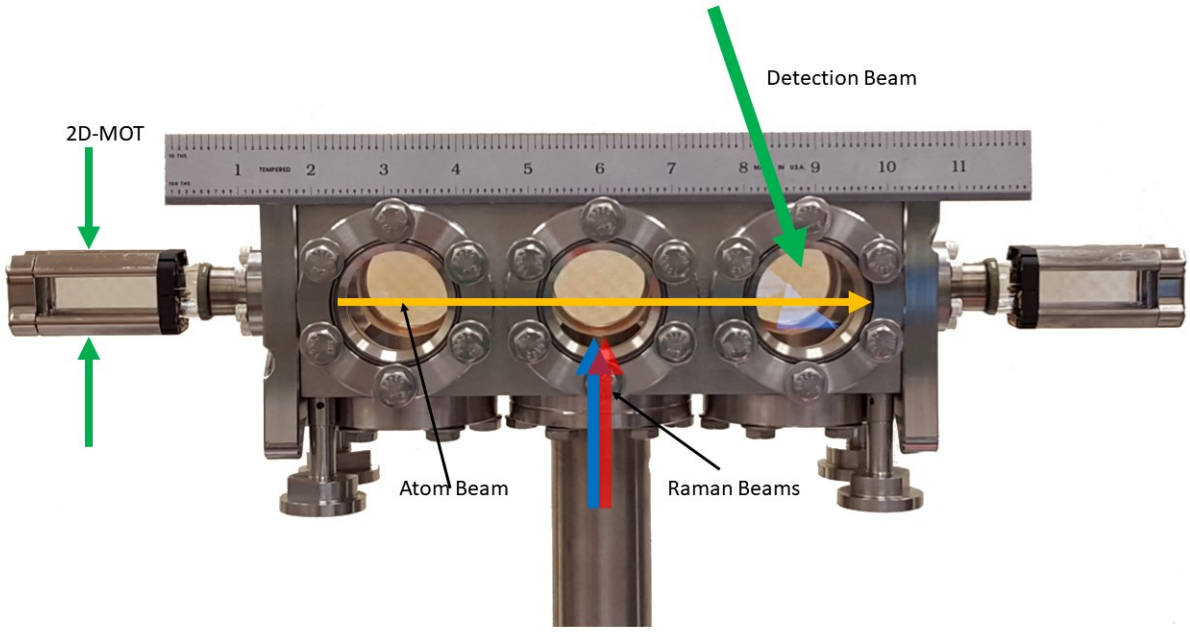

Figure 5.2. The vacuum chamber within which the atom/light interactions occur.

Both of the frequency-shifted Raman beams are generated from the same laser source. A single pass absorption cell is used in the laser setup. Unlike the rest of the lasers in the experiment, there is no need for fine frequency stability since we typically operate with a detuning somewhere

between 100-1000 MHz. On this scale a drift of 1 MHz is insignificant. The Raman beam is oriented in a double single-pass configuration (Figure 5.3) through an acousto-optic modulator (AOM). A single pass produces a beam that is frequency shifted by the radio frequency (RF) driving the AOM. An additional beam passes straight through the AOM and is then incident on a mirror. By retro reflecting this beam we can produce another frequency shifted beam in the opposite direction with a frequency shift of the same magnitude but different direction. Thus the double single-pass configuration produces red/blue beams whose frequencies are shifted down/up and can be controlled by the RF driving the AOM. The red and blue beams are then sent to the experiment using the optics scheme shown in Figure 5.4.

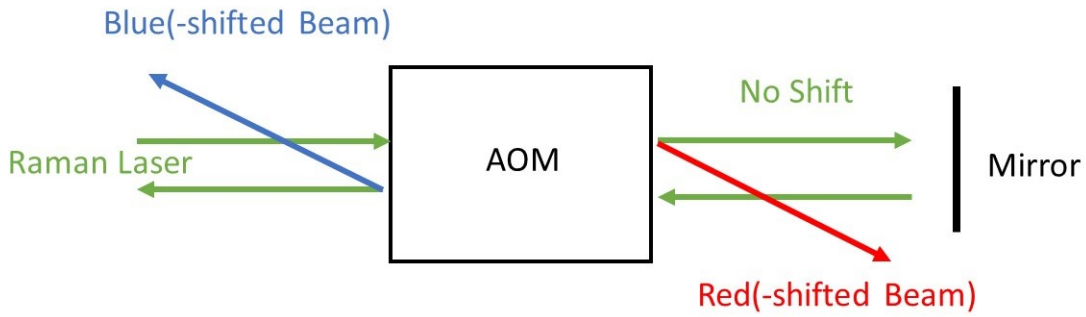

Figure 5.3. Depiction of the optics scheme used to generate two frequency shifted Raman beams from a single laser. During the first pass, the Raman laser is red-shifted by 1517.866 MHz. The second pass causes the beam to be blue-shifted by 1517.866 MHz. The two beams are then sent to the experiment.

5.2 Experiment

The new optics scheme allows the user to control the amount of spatial overlap between the P and the S by use of a mirror on a mount that is able to translate in the direction depicted in the figure. The quarter-wave plates (QWP), half-wave plates (HWP), and polarizing beam splitter (PBS) are used to generate the desired polarization prior to entering the vacuum chamber. The 50/50 cube separates each beam in two and allows for the beams to be overlapped and the light passes through it. The convex and concave lenses are used to change the shape of the beams from small circles to

taller ellipses. Modifying the beams to have elliptical shapes rather than circular is accomplished by cylindrical lenses vise spherical lenses.

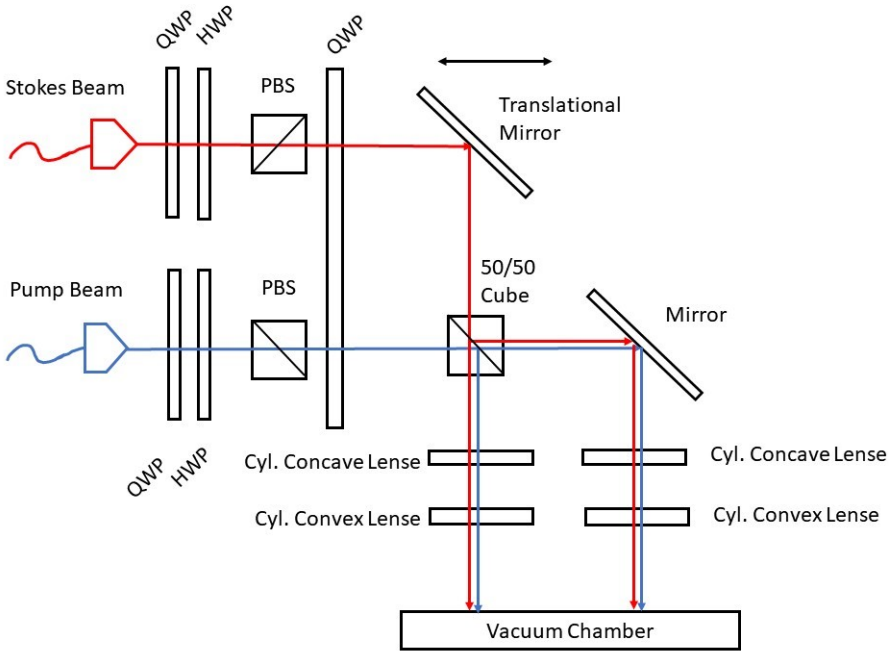

Figure 5.4. Optics schematic to generate the counterintuitive STIRAP orientation of the P and S beams.

For comparison, the previous optics used a two-to-one polarization-maintaining (PM) fiber to combine the red-shifted and blue-shifted light into one spatial beam [16]. The light is then sent through similar optical components before entering the chamber. The optics were simpler, however, there was no way to individually control the amount of overlap between the red and and blue light. This new scheme allows for more degrees of freedom to vary between the condition of complete overlap to the counterintuitive STIRAP configuration. More degrees of freedom increase the difficulty in aligning the optics. We now have to consider the extent of overlap as well as the angle the beams make with respect to each other as they pass through the atom beam. Ideally the two laser beams are perfectly parallel and incident the atom beam at a perfect 90 degree angle. We have proven and verified the effects on the signal if these conditions are not exact.

5.2.1 Angular Tolerance

Ideally, both the red and blue beams intersect the atomic beam at right angles. However, there may be a slight error in the angles as depicted in Figure 5.5.

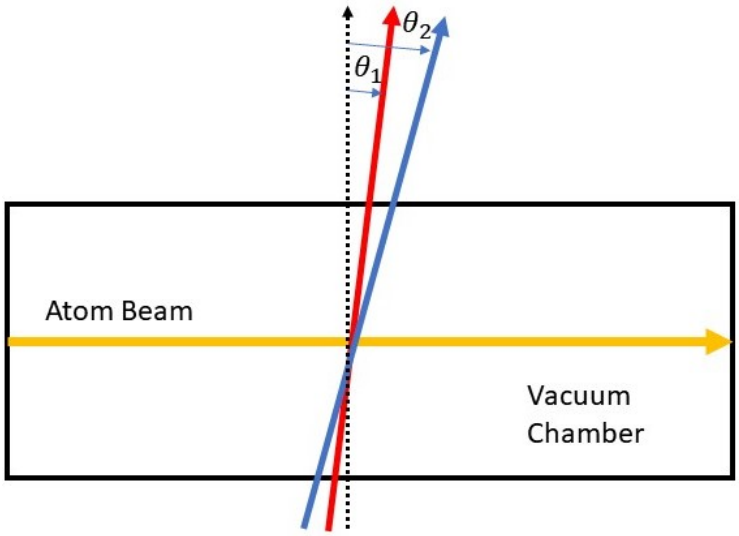

Figure 5.5. Top-down view of the two frequency shifted Raman beams at the point of atom interaction within the vacuum chamber. θ_1 is the angle of the red-shifted light with respect to the normal (dashed-line) while θ_2 corresponds to the blue-shifted light (not drawn to scale).

A Doppler shift of the signal is apparent when an angle exists between the two beams. In this system, a Doppler shift, $\Delta\omega$, is given by

$$\Delta\omega = k_1 v sin\theta_1 - k_2 v sin(\theta_1 + (\theta_2 - \theta_1)), \tag{5.1}$$

where θ_1 and θ_2 are the angles of the red and blue beams respectively. By using trigonometry identities and combining terms, we find that

$$\Delta\omega = k_1 v sin\theta_1 - k_2 v sin\theta_1 - k_2 v cos\theta_1 \delta\theta, \tag{5.2}$$

where $\delta\theta = \theta_2 - \theta_1$. The first two terms will dictate the apparent location of the center frequency when $\delta\theta = 0$ (e.g., when using a two-to-one fiber). Therefore, a frequency shift, $\Delta\omega_{extra}$, is caused

by the angle between the two fields, $\delta\theta$, and is shown to be

$$\Delta\omega_{extra} = k_2 v \delta\theta, \tag{5.3}$$

when θ_1 is small. With typical number used in the lab of $v = 10$ m/s and $\lambda = 780$ nm, we find that we must be within 0.3 degrees in order to have a shift that is less than a scan amplitude of 60kHz. An angle larger than that will move the signal outside the scan window. I verified the Doppler shift in the lab by controlling the translating mirror of the blue-shifted beam to vary this angle at the point of atom beam interaction. The center of the signal shifted up or down in frequency depending on the magnitude and direction of the angle.

5.2.2 Raman Beam Divergence

A study on the effect of Raman beam divergence was done to see the overall impact on the signal. Ideally, the Raman beams would be perfectly collimated as it enters the vacuum chamber. However, there is slight divergence along the path of the atoms which we found to lower the magnitude as well as broadened the signal.

For a Raman spectrum, with its expected Lorentzian profile, we began with

$$I = \frac{\beta^2}{\beta^2 + \delta^2}, \tag{5.4}$$

where 2β is the FWHM and $\delta = \delta_1 = \delta_2$. We included the same Doppler shift equations from earlier and find

$$I = \frac{\beta^2}{\beta^2 + (\delta' + k_2 v sin\theta_2 y - k_1 v sin\theta_1 x)}, \tag{5.5}$$

where δ' is the apparent resonance caused by non-perfect orthogonality without divergence, θ_1 and θ_2 are the angles of the two Raman beams with respect to the perpendicular of the atom beam respectively. Here, x and y are the small variations of those angles, which result in the diverging fields. Equation 5.5 can now be integrated from a maximum to a minimum value in both x and y. A more complete derivation can be found in Section A.3 of the Appendix. Results from this integration are shown in Figure 5.6, where the extent of divergence is varies from 10^{-5° to 1°.

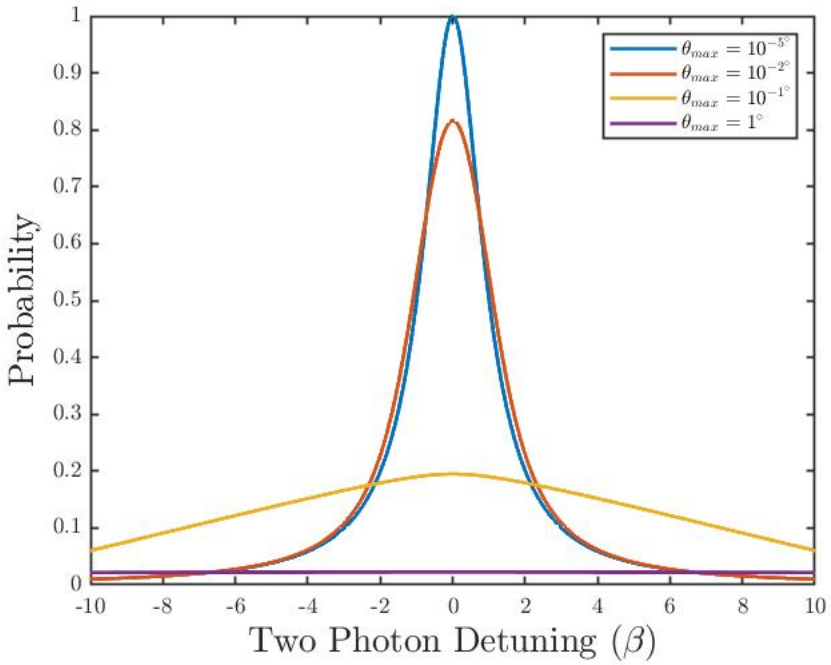

Figure 5.6. The Raman spectrum for an atom of velocity of 10 m/s as the divergence of the Raman field increases. There is strong dependence of the transfer efficiency as Raman beam divergence is increased as there is a loss in magnitude and obvious broadening.

There appears to be a strong relationship between the transfer efficiency of atoms and the magnitude of divergence. The beam divergence with the current optics has been minimized to $\approx 0.01^o$. Greater emphasis will be made on minimizing the Raman beam divergence as the project moves forward.

5.3 Experimental Results

Initial results from the new optics were completed by blocking one of the pairs of beams allowing atom/light interaction with only one pair of beams. In this configuration a Raman spectrum is generated instead of the Ramsey interference which uses two pulses. The new optics provided the results shown on the left in Figure 5.1 which show a Raman signal similar to the signal generated from the previous version of optics. We expect the loss of magnitude and broadening is a result of Raman beam divergence, which had not been optimized.

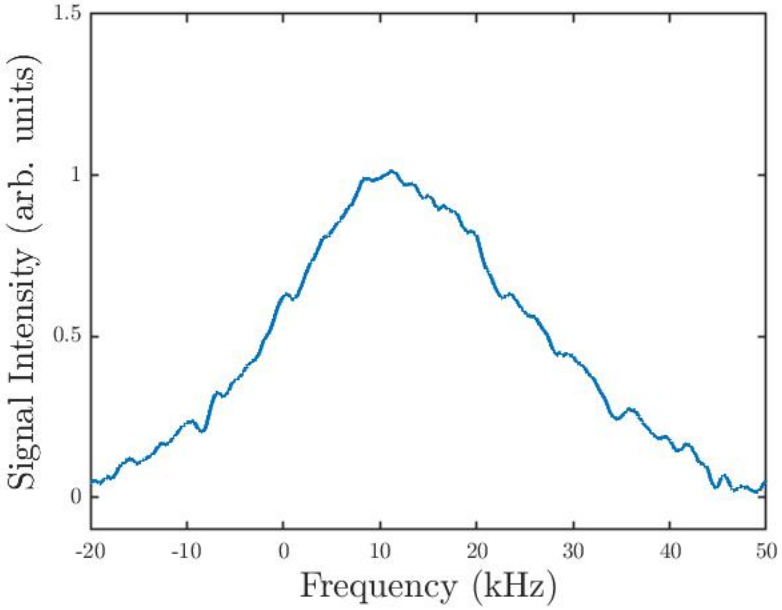

Figure 5.7. Experimental results of a Raman spectrum with the new optics (see Figure 5.4) scheme with control of both the red and blue-shifted light.

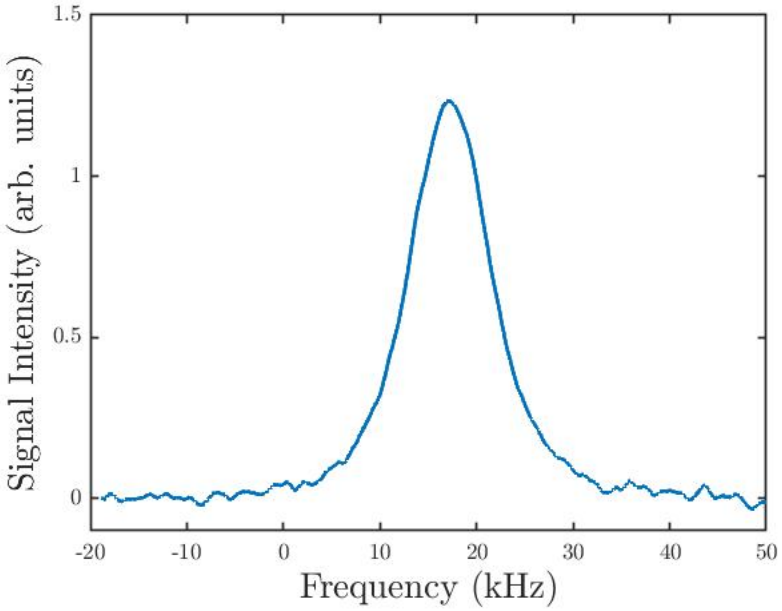

Figure 5.8. Experimental results of a Raman spectrum with the previous optics scheme using a two-to-one fiber.

The new optics have provided promising results in initial tests, however, the design introduces far more degrees of freedom all of which need to be optimized. More time must be spent in optimizing the new system to find a more stable signal as we forward in development of our atomic gyroscope. Additionally, we expect a combination of power broadening and Raman beam divergence to be present in the recent signal which would explain the wider Raman spectrum.

THIS PAGE INTENTIONALLY LEFT BLANK

CHAPTER 6:
Outlook and Conclusions

Our results are a benefit to the Navy as they build the foundation for a viable replacement to RLGs. Naval ships and aircraft will be better suited to operate in a GPS denied environment whether it is a result of war or simply due to a submarine operating submerged. Atomic sensors have been proven to be more sensitive than their counterparts as well as less prone to drift. The continuous-beam design of the sensor will be pivotal in future adaptations to provide a compact and battle hardened inertial sensor. It will be more reliable and better for platform navigation as the Navy continues to patrol the world's seas and skies.

6.1 Outlook and Conclusion: Model

In summary, we have modeled the application of stimulated Raman adiabatic passage (STIRAP) within a continuous beam atomic gyroscope by use of both a Schrödinger picture and and by use of the density matrix. Our model accounts for velocity averaging as a result or the continuous atomic beam. The model provided valuable information on the optimal separation between the pump (P) and Stokes (S) beams as well as insight into the effects of single photon detuning on the system. The sensor must operate off single photon resonance to fall into the adiabatic regime and thus allow for a controlled transfer of population of atoms from one state to another. Additionally, initial models indicate that there is a benefit in the implementation of STIRAP into the gyroscope as better coherence is expected. Our model shows greater contrast in the Ramsey interference pattern when STIRAP is implemented when compared to the conventional configuration. This would result in a more robust sensor to system variations which would improve overall performance.

The next phase of model development will be to incorporate the third set of Raman beams to capture the full $\pi/2 - \pi - \pi/2$ pulse configuration needed for our gyroscope. We expect the π pulse in the STIRAP configuration to be far more robust to the spread in atom velocity. We are working on ways to optimize the code to reduce the current computation time. We believe there may be analytical solutions we could use to replace the need to solve the differential equations numerically, thus greatly improving the run-time of the model. The current code with only two pairs of beams requires >48hrs to complete the model of Ramsey interference on an average laptop CPU. This time will only increase as we add the third pair of Raman beams.

We are also working on a method to quantify the differences between STIRAP and the conventional

configuration. Contrast is typically used when characterizing interference patterns, so a more convenient way to define contrast will be useful for in the future. Ultimately, the model would output a value or a single parameter from a resulting Ramsey or spin echo interference pattern that would capture the quality of the interference pattern. This value will change based of system parameters and thus can be optimized to find the best configuration for the experiment.

6.2 Outlook and Conclusion: Experiment

Early experimental results with the new optics scheme show Raman spectra of similar magnitude as the signal from the previous configuration. There is more control of the individual red (Stokes) and blue (pump) beams allowing for more precise optimization of the resulting interference patterns. However, the more control points have added more points to be optimized. A total system optimization will need to be done to ensure the best signal is used when we begin to measure rotation rate. More work needs to be placed into Raman beam divergence since we expect this as the major contributor to the signal broadening. Future steps within the experiment include the addition of a second set of pulses to create the Ramsey spectrum to validate the models.

Once a Ramsey spectrum has been optimized, the optics would need to be redesigned to incorporate the third set of beams. This will be no small task since the three sets of beams will need the same ability to adjust P vs S separation while allowing for the middle π pulse beams to have a larger peak Rabi frequency independent of the two other sets. With all three sets of Raman beams in the system, tests can then progress towards actual rotation and acceleration measurements. This will require a second, anti-parallel atomic beam [16] to provide the ability to distinguish between the rotation and acceleration.

Our group is also looking at other ways to improve signal stability. The addition of STIRAP appears to be a method to improve the stability while others are working on an improved method of laser locking and an upgraded 2D-MOT apparatus. This will become very important once the sensor is expected to run for long periods of time and small fluctuations compound over time impacting the sensor's performance.

APPENDIX: Derivations

A.1 Schrödinger Approach Theory

A three-level atom can be modeled using the Schrödinger approach starting with the semi-classical Hamiltonian

$$\mathcal{H} = \hbar\Delta \left|2\right\rangle \left\langle 2\right| + \hbar\omega_{13} \left|3\right\rangle \left\langle 3\right| - \hat{\boldsymbol{\mu}} \cdot \boldsymbol{E}, \tag{A.1a}$$

where

$$\hat{\boldsymbol{\mu}} = \boldsymbol{\mu}_{23} \left|2\right\rangle \left\langle 3\right| + \boldsymbol{\mu}_{13} \left|1\right\rangle \left\langle 3\right| + \boldsymbol{\mu}_{23}^{*} \left|3\right\rangle \left\langle 2\right| + \boldsymbol{\mu}_{13}^{*} \left|3\right\rangle \left\langle 1\right|, \tag{A.1b}$$

and

$$\boldsymbol{E} = \mathcal{E}_1 \boldsymbol{\epsilon}_1 e^{i(\omega_1 t - k_1 z)} + \mathcal{E}_2 \boldsymbol{\epsilon}_2 e^{i(\omega_2 t - k_2 z)}. \tag{A.1c}$$

In the above equations, $\hat{\boldsymbol{\mu}}$ represents the atomic dipole moment and $\boldsymbol{E}$ is the electric field. The total laser field consists of two modes of amplitude $\mathcal{E}_i$, frequencies ω_i, wave number k_i, and polarization vector $\boldsymbol{\epsilon}_i$ $(i = 1, 2)$ The last terms of the Hamiltonian are determined by multiplying Equation A.1b and Equation A.1c to yield

$$\begin{aligned} \boldsymbol{\mu} \cdot \boldsymbol{E} = {} & \boldsymbol{\mu}_{23} \cdot \boldsymbol{\epsilon}_2^{*} e^{i(\omega_2 t - k_2 z)} \left|2\right\rangle \left\langle 3\right| + \boldsymbol{\mu}_{13} \cdot \boldsymbol{\epsilon}_1^{*} e^{i(\omega_1 t - k_1 z)} \left|1\right\rangle \left\langle 3\right| + \\ & \boldsymbol{\mu}_{23}^{*} \cdot \boldsymbol{\epsilon}_2 e^{-i(\omega_2 t - k_2 z)} \left|3\right\rangle \left\langle 2\right| + \boldsymbol{\mu}_{13}^{*} \cdot \boldsymbol{\epsilon}_1 e^{-i(\omega_1 t - k_1 z)} \left|3\right\rangle \left\langle 1\right|, \end{aligned} \tag{A.2}$$

where terms proportional to $\boldsymbol{\mu}^{*} \cdot \boldsymbol{\epsilon}^{*}$ or $\boldsymbol{\mu} \cdot \boldsymbol{\epsilon}$ are thrown out because they eventually lea to terms that average to zero.

A unique way to simplify Equation A.2 is to introduce the Rabi frequency, Ω. The Rabi frequency is the rate at which the atom oscillates between the ground state and excited state and is defined as

$$\Omega_i = \frac{2\boldsymbol{\mu}_{i3}^{*} \cdot \boldsymbol{\epsilon}_i \mathcal{E}_i}{\hbar}. \qquad (i = 1, 2) \tag{A.3}$$

The simplification of Equation A.2 yields

$$\begin{aligned}\boldsymbol{\mu}\cdot\boldsymbol{E} = &\frac{1}{2}\hbar\Omega_2^* e^{i(\omega_2 t-k_2 z)}\left|2\right\rangle\left\langle 3\right| + \frac{1}{2}\hbar\Omega_1^* e^{i(\omega_1 t-k_1 z)}\left|1\right\rangle\left\langle 3\right| \\ &+\frac{1}{2}\hbar\Omega_2 e^{-i(\omega_2 t-k_2 z)}\left|3\right\rangle\left\langle 2\right| + \frac{1}{2}\hbar\Omega_1 e^{-i(\omega_1 t-k_1 z)}\left|3\right\rangle\left\langle 1\right|.\end{aligned} \tag{A.4}$$

Finally, the combination of $\boldsymbol{\mu}$ and $\boldsymbol{E}$ is added into the Hamiltonian to give

$$\begin{aligned}H = \hbar\Delta\left|2\right\rangle\left\langle 2\right| + \hbar\omega_{13}\left|3\right\rangle\left\langle 3\right| - \frac{1}{2}\hbar\Omega_2^* e^{i(\omega_2 t-k_2 z)}\left|2\right\rangle\left\langle 3\right| - \frac{1}{2}\hbar\Omega_1^* e^{i(\omega_1 t-k_1 z)}\left|1\right\rangle\left\langle 3\right| \\ -\frac{1}{2}\hbar\Omega_2 e^{-i(\omega_2 t-k_2 z)}\left|3\right\rangle\left\langle 2\right| - \frac{1}{2}\hbar\Omega_1 e^{-i(\omega_1 t-k_1 z)}\left|3\right\rangle\left\langle 1\right|.\end{aligned} \tag{A.5}$$

Now that the Hamiltonian has been constructed, the time dependent Schrodinger equation,

$$i\hbar\frac{\partial\psi}{\partial t} = H\psi, \tag{A.6}$$

is ready to be solved.

The state of the atom at any time, t, can be written in terms of the atomic basis state as

$$\left|\psi(t)\right\rangle = c_1(t)\left|1\right\rangle + c_2(t)\left|2\right\rangle + c_3(t)\left|3\right\rangle. \tag{A.7}$$

The right side of the Schrodinger equation is found by multiplying Equation A.5 by Equation A.7. The result is shown here as

$$\begin{aligned}H * \left|\psi(t)\right\rangle = \hbar\Delta_1 c_2(t)\left|2\right\rangle + \hbar\omega_{13}c_3(t)\left|3\right\rangle - \frac{1}{2}\hbar\Omega_2^* e^{i(\omega_2 t-k_2 z)}c_3(t)\left|2\right\rangle - \frac{1}{2}\hbar\Omega_1^* e^{i(\omega_1 t-k_1 z)}c_3(t)\left|1\right\rangle \\ -\frac{1}{2}\hbar\Omega_2^* e^{-i(\omega_2 t-k_2 z)}c_2(t)\left|3\right\rangle - \frac{1}{2}\hbar\Omega_1^* e^{-i(\omega_1 t-k_1 z)}c_1(t)\left|3\right\rangle.\end{aligned} \tag{A.8}$$

Solving the left side of the Schrodinger equation involves a time derivative of Equation A.7 and multiplying each term by $i\hbar$ to give

$$i\hbar\frac{\partial\psi}{\partial t} = i\hbar\dot{c_1}(t)\left|1\right\rangle + i\hbar\dot{c_2}(t)\left|2\right\rangle + i\hbar\dot{c_3}(t)\left|3\right\rangle. \tag{A.9}$$

We now multiply Equation A.9 by $\langle i|$, where $i = 1, 2, 3$, and get

$$
\begin{aligned}
i\hbar\dot{c_1}(t) &= -\frac{1}{2}\hbar\Omega_1^* e^{i(\omega_1 t - k_1 z)} c_3(t), && \text{(A.10a)}\\
i\hbar\dot{c_2}(t) &= \hbar\Delta_1 c_2(t) - \frac{1}{2}\hbar\Omega_2^* e^{i(\omega_2 t - k_2 z)} c_3(t), && \text{(A.10b)}\\
i\hbar\dot{c_3}(t) &= \hbar\omega_{13} c_3(t) - \frac{1}{2}\hbar\Omega_2^* e^{-i(\omega_1 t - k_1 z)} c_2(t) - \frac{1}{2}\hbar\Omega_1 e^{-i(\omega_1 t - k_1 z)} c_1(t). && \text{(A.10c)}
\end{aligned}
$$

Simplifying the equations further, the result is three coupled ordinary differential equations given by

$$
\begin{aligned}
\dot{c_1}(t) &= \frac{i}{2}\Omega_1^* e^{i(\omega_1 t - k_1 z)} c_3(t), && \text{(A.11a)}\\
\dot{c_2}(t) &= -i\Delta_1 c_2 + \frac{i}{2}\Omega_2^* e^{i(\omega_2 t - k_2 z)} c_3(t), && \text{(A.11b)}\\
\dot{c_3}(t) &= -i\omega_{13} c_3(t) + \frac{i}{2}\Omega_2 e^{-i(\omega_2 t - k_2 z)} c_2(t) + \frac{i}{2}\Omega_1 e^{-i(\omega_1 t - k_1 z)} c_1(t). && \text{(A.11c)}
\end{aligned}
$$

An approximation now must be made to simplify the differential equations into a form that is numerically integrable. This is accomplished by applying the transformation

$$
\begin{aligned}
c_1 &= \tilde{c_1}, && \text{(A.12a)}\\
c_2 &= \tilde{c_2} e^{-i((\omega_1 - \omega 2)t - (k_1 - k_2)z)}, && \text{(A.12b)}\\
c_3 &= \tilde{c_3} e^{-i(\omega_1 t - k_1 z)}, && \text{(A.12c)}
\end{aligned}
$$

which changes the system into a frame rotating at ω_L. By applying the RWA, the counter-rotating terms are thrown out.

Taking the time derivative of the new equations, we get

$$
\begin{aligned}
\dot{c_1} &= \dot{\tilde{c_1}},\\
\dot{c_2} &= -i[(\omega_1 - \omega_2) - (k_1 - k_2)v)]\tilde{c_2} e^{-i((\omega_1 - \omega 2)t - (k_1 - k_2)z)} + \dot{\tilde{c_2}} e^{-i((\omega_1 - \omega 2)t - (k_1 - k_2)z)},\\
\dot{c_3} &= -i(\omega_1 - kv)\tilde{c_3} e^{-i(\omega_1 t - k_1 z)} + \dot{\tilde{c_3}} e^{-i(\omega_1 t - k_1 z)}.
\end{aligned}
$$

Another set of time derivatives are found by substituting the transformed amplitudes into the right hand side of Equations A.11a, A.11b, and A.11c.

$$\begin{aligned}
\dot{c_1}(t) &= \frac{i}{2}\Omega_1^* e^{i(\omega_1 t - k_1 z)}\tilde{c_3}e^{-i(\omega_1 t - k_1 z)} \\
\dot{c_2}(t) &= -i\Delta_1 \tilde{c_2} e^{-i((\omega_1-\omega_2)t-(k_1-k_2)z)} + \frac{i}{2}\Omega_2^* e^{i(\omega_2 t - k_2 z)}\tilde{c_3} \\
\dot{c_3}(t) &= -i\omega_{13}\tilde{c_3}e^{-i(\omega_1 t - k_1 z)} + \frac{i}{2}\Omega_2 e^{-i(\omega_2 t - k_2 z)}\tilde{c_2}e^{-i((\omega_1-\omega_2)t-(k_1-k_2)z)} + \frac{i}{2}\Omega_1 e^{-i(\omega_1 t - k_1 z)}\tilde{c_1}
\end{aligned}$$

The two sets of equations of time derivatives are equated to each other. The relationships are then rearranged to solve for $\dot{\tilde{c}}$. Finally, the exponentials are simplified and we are left with

$$\begin{aligned}
\dot{\tilde{c_1}} &= \frac{i}{2}\Omega_1^*\tilde{c_3}, \\
\dot{\tilde{c_2}} &= -i[\Delta_1 - (\omega_1 - \omega_2) + (k_1 - k_2)v]\tilde{c_2} + \frac{i}{2}\Omega_2^*\tilde{c_3}, \\
\dot{\tilde{c_3}} &= -i(\omega_{13} - \omega_1 + k_1 v)\tilde{c_3} + \frac{i}{2}\Omega_2\tilde{c_2} + \frac{i}{2}\Omega_1\tilde{c_1}.
\end{aligned}$$

Noting that

$$\Delta_1 = \omega_{13} - \omega_{23} \tag{A.13}$$

and that the individual laser detuning can be written as

$$\begin{aligned}
\delta_1 &= \omega_1 - \omega_{13} \\
\delta_2 &= \omega_2 - \omega_{23},
\end{aligned}$$

we then have a useful relationship involving single photon detuning of the state 1 and state 2 transitions given by

$$\Delta_1 - (\omega_1 - \omega_2) = \delta_2 - \delta_1. \tag{A.14}$$

Thus, our final set of coupled differential equations is

$$\dot{\tilde{c}_1} = \frac{i}{2}\Omega_1^*\tilde{c_3}, \tag{A.15a}$$

$$\dot{\tilde{c}_2} = -i[(\delta_2 - \delta_1) - (k_2 - k_1)v]\tilde{c_2} + \frac{i}{2}\Omega_2^*\tilde{c_3} \tag{A.15b}$$

$$\dot{\tilde{c}_3} = i(\delta_1 - k_1 v)\tilde{c_3} + \frac{i}{2}\Omega_2\tilde{c_2} + \frac{i}{2}\Omega_1\tilde{c_1}. \tag{A.15c}$$

The final Ψ matrix is shown to represent each state in the new rotating frame shown by

$$\Psi = \begin{bmatrix} \tilde{c_1} \\ \tilde{c_2} \\ \tilde{c_3} \end{bmatrix}. \tag{A.16}$$

The right side of Equations A.15b, A.15c, and A.15c is grouped into a matrix labeled L.

$$L = \begin{bmatrix} 0 * \tilde{c_1} & 0 * \tilde{c_2} & \frac{i}{2}\Omega_1^*\tilde{c_3} \\ 0 * \tilde{c_1} & -i(\delta_2 - \delta_1)\tilde{c_2} & \frac{i}{2}\Omega_2^*\tilde{c_3} \\ \frac{i}{2}\Omega_1\tilde{c_1} & \frac{i}{2}\Omega_2\tilde{c_2} & i\delta_1\tilde{c_3} \end{bmatrix} \tag{A.17}$$

This matrix can be solved numerically using MATLAB.

A.2 Density Matrix Theory

The three-level atom is investigated using the density matrix approach which permits spontaneous decay to be included in the calculations. Again, the Hamiltonian is

$$\mathcal{H} = \hbar\Delta \left|2\right\rangle \left\langle 2\right| + \hbar\omega_{13} \left|3\right\rangle \left\langle 3\right| - \boldsymbol{\mu} \cdot \boldsymbol{E}, \tag{A.18}$$

where

$$\boldsymbol{\mu} = \boldsymbol{\mu}_{23} \left|2\right\rangle \left\langle 3\right| + \boldsymbol{\mu}_{13} \left|1\right\rangle \left\langle 3\right| + \boldsymbol{\mu}_{23}^* \left|3\right\rangle \left\langle 2\right| + \boldsymbol{\mu}_{13}^* \left|3\right\rangle \left\langle 1\right|, \tag{A.19}$$

and

$$\boldsymbol{E} = \mathcal{E}_1\boldsymbol{\epsilon}_1 e^{i(\omega_1 t - k_1 z)} + \mathcal{E}_2\boldsymbol{\epsilon}_2 e^{i(\omega_2 t - k_2 z)}. \tag{A.20}$$

In writing Equation A.19, it is implicitly assumed that there is no optical transition between states$|1\rangle$ and $|2\rangle$. The laser fields have polarization, which is denoted by the symbol $\boldsymbol{\epsilon}_i$. The Schrodinger equation describes how states evolve in time while the Von Neuman equation describes how the density operator evolves in time. The Von Neuman equation of motion is again given as

$$\dot{\rho} = -\frac{i}{\hbar}\left[\mathcal{H}, \rho\right].$$

Substitution of the Hamiltonian, Equation A.18 into the Von Neuman equation of motion yields,

$$\begin{aligned}
\dot{\rho} &= -i\Delta\left(|2\rangle\langle 2|\,\rho - \rho\,|2\rangle\langle 2|\right) - i\omega_{13}\left(|3\rangle\langle 3|\,\rho - \rho\,|3\rangle\langle 3|\right) \\
&\quad + \frac{i}{\hbar}\left[\mu_{23}\left(|2\rangle\langle 3|\,\rho - \rho\,|2\rangle\langle 3|\right) + \mu_{13}\left(|1\rangle\langle 3|\,\rho - \rho\,|1\rangle\langle 3|\right)\right] \cdot E_T(z,t) \\
&\quad + \frac{i}{\hbar}\left[\mu_{23}^*\left(|3\rangle\langle 2|\,\rho - \rho\,|3\rangle\langle 2|\right) + \mu_{13}^*\left(|3\rangle\langle 1|\,\rho - \rho\,|3\rangle\langle 1|\right)\right] \cdot E_T(z,t).
\end{aligned}$$

By projecting the density operator onto the states $\langle i|$ and $|j\rangle$, we can write the equations for the components of the density operator as

$$\begin{aligned}
\dot{\rho}_{22} &= \frac{i}{\hbar}\left[\mu_{23}\rho_{32} - \mu_{23}^*\rho_{23}\right] \cdot E_T(z,t) \\
\dot{\rho}_{33} &= \frac{i}{\hbar}\left[\mu_{23}^*\rho_{23} + \mu_{13}^*\rho_{13} - \mu_{23}\rho_{32} - \mu_{23}\rho_{31}\right] \cdot E_T(z,t) \\
\dot{\rho}_{23} &= i\left(\omega_{13} - \Delta\right)\rho_{23} + \frac{i}{\hbar}\left[\mu_{23}\left(\rho_{33} - \rho_{22}\right)\mu_{13}\rho_{21}\right] \cdot E_T(z,t) \\
\dot{\rho}_{13} &= i\omega_{13}\rho_{13} + \frac{i}{\hbar}\left[\mu_{13}\left(\rho_{33} - \rho_{11}\right) - \mu_{23}\rho_{12}\right] \cdot E_T(z,t) \\
\dot{\rho}_{12} &= i\Delta\rho_{12} + \frac{i}{\hbar}\left[\mu_{13}\rho_{32} - \mu_{23}^*\rho_{13}\right] \cdot E_T(z,t).
\end{aligned}$$

The next step is to remove the explicit time dependence. The following transformation is used to represent the system with slowly varying quantities denoted by the tilde. The expressions are given

as

$$\begin{aligned}
\rho_{ii}(t) &= \tilde{\rho}_{ii}(t) \qquad\qquad (i = 1,2,3) \\
\rho_{13}(t) &= \tilde{\rho}_{13}(t)e^{-\imath(\omega_1 t - k_1 z)} \\
\rho_{23}(t) &= \tilde{\rho}_{23}(t)e^{-\imath(\omega_2 t - k_2 z)} \\
\rho_{12}(t) &= \tilde{\rho}_{12}(t)e^{i[(\omega_1-\omega_2)t-(k_1-k_2)z]}.
\end{aligned}$$

Another approximation is made to simplify the equations. Each optical field interacts with only one transition. This is not an approximation based on large detuning. It can be made exact by taking $\mu_{23}^* \cdot \epsilon_1 = \mu_{13}^* \cdot \epsilon_2 = 0$, which can be done in principle by choosing the correct transitions and laser polarizations. The density equations are now

$$\begin{aligned}
\dot{\tilde{\rho}}_{22} &= \frac{i}{\hbar}\left[\mu_{23}\cdot\epsilon_2^*\mathcal{E}_2^*\tilde{\rho}_{32} - \mu_{23}^*\cdot\epsilon_2\mathcal{E}_2\tilde{\rho}_{23}\right] \\
\dot{\tilde{\rho}}_{33} &= \frac{i}{\hbar}\left[\mu_{23}^*\cdot\epsilon_2\mathcal{E}_2\tilde{\rho}_{23} + \mu_{13}^*\cdot\epsilon_1\mathcal{E}_1\tilde{\rho}_{13} - \mu_{23}\cdot\epsilon_2^*\mathcal{E}_2^*\tilde{\rho}_{32} - \mu_{13}\cdot\epsilon_1^*\mathcal{E}_1^*\tilde{\rho}_{31}\right] \\
\dot{\tilde{\rho}}_{23} &= i\left[\omega_{23} - \omega_2 + k_2 v\right]\tilde{\rho}_{23} + \frac{i}{\hbar}\left[\mu_{23}\cdot\epsilon_2^*\mathcal{E}_2^*\left(\tilde{\rho}_{33}-\tilde{\rho}_{22}\right) - \mu_{13}\cdot\epsilon_1^*\mathcal{E}_1^*\tilde{\rho}_{21}\right] \\
\dot{\tilde{\rho}}_{13} &= i\left[\omega_{13} - \omega_1 + k_1 v\right]\tilde{\rho}_{13} + \frac{i}{\hbar}\left[\mu_{13}\cdot\epsilon_1^*\mathcal{E}_1^*\left(\tilde{\rho}_{33}-\tilde{\rho}_{11}\right) - \mu_{23}\cdot\epsilon_2^*\mathcal{E}_2^*\tilde{\rho}_{12}\right] \\
\dot{\tilde{\rho}}_{12} &= i\left[\Delta - (\omega_1-\omega_2) + (k_1-k_2)\,v\right]\tilde{\rho}_{12} + \frac{i}{\hbar}\left[\mu_{13}\cdot\epsilon_1^*\mathcal{E}_1^*\tilde{\rho}_{32} - \mu_{23}^*\cdot\epsilon_2\mathcal{E}_2\tilde{\rho}_{13}\right].
\end{aligned}$$

To further simplify the equations, Rabi frequency (Equation A.3) and single photon dutuning (Equation A.14) terms are used to consolidate variables. With these substitutions, we get

$$\begin{aligned}
\dot{\tilde{\rho}}_{22} &= \frac{i}{2}\left(\Omega_2^*\tilde{\rho}_{32} - \Omega_2\tilde{\rho}_{23}\right) \\
\dot{\tilde{\rho}}_{33} &= \frac{i}{2}\left(\Omega_2\tilde{\rho}_{23} + \Omega_1\tilde{\rho}_{13} - \Omega_2^*\tilde{\rho}_{32} - \Omega_1^*\tilde{\rho}_{31}\right) \\
\dot{\tilde{\rho}}_{23} &= i\left(k_2 v - \delta_2\right)\tilde{\rho}_{23} + \frac{i}{2}\left[\Omega_2^*\left(\tilde{\rho}_{33}-\tilde{\rho}_{22}\right) - \Omega_1^*\tilde{\rho}_{21}\right] \\
\dot{\tilde{\rho}}_{13} &= i\left(k_1 v - \delta_1\right)\tilde{\rho}_{13} + \frac{i}{2}\left[\Omega_1^*\left(\tilde{\rho}_{33}-\tilde{\rho}_{11}\right) - \Omega_2^*\tilde{\rho}_{12}\right] \\
\dot{\tilde{\rho}}_{12} &= i\left[\left(\delta_2-\delta_1\right) + \left(k_1-k_2\right)v\right]\tilde{\rho}_{12} + \frac{i}{2}\left[\Omega_1^*\tilde{\rho}_{32} - \Omega_2\tilde{\rho}_{13}\right].
\end{aligned}$$

Incoherent decay is introduced by writing

$$\begin{aligned}
\dot{\tilde{\rho}}_{33} &= -\left(W_{32}+W_{31}\right)\tilde{\rho}_{33} \\
\dot{\tilde{\rho}}_{22} &= W_{32}\tilde{\rho}_{33}+W_{12}\tilde{\rho}_{11}-W_{21}\tilde{\rho}_{22} \\
\dot{\tilde{\rho}}_{ij} &= -\gamma_{ij}\tilde{\rho}_{ij}.
\end{aligned}$$

W_{ij} is the decay from level i to level j. Upward incoherent transitions between ground states (i.e. W_{12}) is not retained. Upward transitions of optical frequencies are assumed to be zero (i.e. $W_{13} = W_{23} = 0$). γ_{ij} is the polarization decay rate for the $i \rightarrow j$ transition. In the radiative limit, this is given by

$$\gamma_{ij} = \frac{1}{2}\sum_{k=1}^{3}\left[W_{ik}+W_{jk}\right]. \tag{A.21}$$

Furthermore, the system is assumed to be closed. Therefore, $\tilde{\rho}_{11}+\tilde{\rho}_{22}+\tilde{\rho}_{33} = 1$. Thus, $\tilde{\rho}_{11}$ can be eliminated from the equations leaving a resultant equation of

$$\begin{aligned}
\dot{\tilde{\rho}}_{22} &= W_{32}\tilde{\rho}_{33}+W_{12}\left(1-\tilde{\rho}_{22}-\tilde{\rho}_{33}\right)-W_{21}\tilde{\rho}_{22} \\
&= \left(W_{32}-W_{12}\right)\tilde{\rho}_{33}-\left(W_{12}+W_{21}\right)\tilde{\rho}_{22}+W_{12}.
\end{aligned}$$

The final set of equations to be integrated can be shown to be

$$\begin{aligned}
\dot{\tilde{\rho}}_{22} &= \left(W_{32}-W_{12}\right)\tilde{\rho}_{33}-\left(W_{12}+W_{21}\right)\tilde{\rho}_{22}+\frac{i}{2}\left(\Omega_2^*\tilde{\rho}_{32}-\Omega_2\tilde{\rho}_{23}\right)+W_{12} \\
\dot{\tilde{\rho}}_{33} &= -\left(W_{31}+W_{32}\right)\tilde{\rho}_{33}+\frac{i}{2}\left(\Omega_2\tilde{\rho}_{23}+\Omega_1\tilde{\rho}_{13}-\Omega_2^*\tilde{\rho}_{32}-\Omega_1^*\tilde{\rho}_{31}\right) \\
\dot{\tilde{\rho}}_{23} &= -\left[\gamma_{23}+i\left(\delta_2-k_2v\right)\right]\tilde{\rho}_{23}+\frac{i}{2}\left[\Omega_2^*\left(\tilde{\rho}_{33}-\tilde{\rho}_{22}\right)-\Omega_1^*\tilde{\rho}_{21}\right] \\
\dot{\tilde{\rho}}_{13} &= -\left[\gamma_{13}+i\left(\delta_1-k_1v\right)\right]\tilde{\rho}_{13}+\frac{i}{2}\left[\Omega_1^*\left(2\tilde{\rho}_{33}+\rho_{22}-1\right)-\Omega_2^*\tilde{\rho}_{12}\right] \\
\dot{\tilde{\rho}}_{12} &= -\left\{\gamma_{12}-i\left[\left(\delta_2-\delta_1\right)-\left(k_2-k_1\right)v\right]\right\}\tilde{\rho}_{12}+\frac{i}{2}\left[\Omega_1^*\tilde{\rho}_{32}-\Omega_2\tilde{\rho}_{13}\right].
\end{aligned} \tag{A.22}$$

Now, for programming purposes, a column vector is defined as

$$\psi = [\tilde{\rho}_{12}\ \tilde{\rho}_{13}\ \tilde{\rho}_{21}\ \tilde{\rho}_{22}\ \tilde{\rho}_{23}\ \tilde{\rho}_{31}\ \tilde{\rho}_{32}\ \tilde{\rho}_{33}\ ]^T\ .$$

Next, we can write out each term of the ψ matrix in terms of a derivative in time to give us

$$\begin{aligned}
\dot{\psi}_1 &= -\{\gamma_{12} - i\left[(\delta_2 - \delta_1) - (k_2 - k_1)\, v\right]\}\psi_1 + \frac{i}{2}\left[\Omega_1^*\psi_7 - \Omega_2\psi_2\right] \\
\dot{\psi}_2 &= -\left[\gamma_{13} + i\,(\delta_1 - k_1 v)\right]\psi_2 + \frac{i}{2}\left[\Omega_1^*\,(2\psi_8 + \psi_4 - 1) - \Omega_2^*\psi_1\right] \\
\dot{\psi}_3 &= -\{\gamma_{12} + i\left[(\delta_2 - \delta_1) - (k_2 - k_1)\, v\right]\}\psi_3 - \frac{i}{2}\left[\Omega_1\psi_5 - \Omega_2^*\psi_6\right] \\
\dot{\psi}_4 &= (W_{32} - W_{12})\,\psi_8 - (W_{12} + W_{21})\,\psi_4 + \frac{i}{2}\left(\Omega_2^*\psi_7 - \Omega_2\psi_5\right) + W_{12} \\
\dot{\psi}_5 &= -\left[\gamma_{23} + i\,(\delta_2 - k_2 v)\right]\psi_5 + \frac{i}{2}\left[\Omega_2^*\,(\psi_8 - \psi_4) - \Omega_1^*\psi_3\right] \\
\dot{\psi}_6 &= -\left[\gamma_{13} - i\,(\delta_1 - k_1 v)\right]\psi_6 - \frac{i}{2}\left[\Omega_1\,(2\psi_8 + \psi_4 - 1) - \Omega_2\psi_3\right] \\
\dot{\psi}_7 &= -\left[\gamma_{23} - i\,(\delta_2 - k_2 v)\right]\psi_7 - \frac{i}{2}\left[\Omega_2\,(\psi_8 - \psi_4) - \Omega_1\psi_1\right] \\
\dot{\psi}_8 &= -(W_{31} + W_{32})\,\psi_8 + \frac{i}{2}\left(\Omega_2\psi_5 + \Omega_1\psi_2 - \Omega_2^*\psi_7 - \Omega_1^*\psi_6\right),
\end{aligned} \tag{A.23}$$

which are the final coupled differential equations for the density matrix model.

A.3 Raman Beam Divergence

The Raman resonance is given by

$$I = \frac{\beta^2}{\beta^2 + \delta^2}, \tag{A.24}$$

where 2β is the FWHM of the Lorentzian curve and δ is the detuning. We have established that

$$\delta = \delta_2 - \delta_1 = (\omega_2 - \omega_{23}) - (\omega_1 - \omega_{13}), \tag{A.25}$$

but we must include Doppler shift due to imperfect orthogonality. For this, we write

$$\omega_1 \rightarrow \omega_1' - k_1 v cos\theta_1 \tag{A.26}$$
$$\omega_2 \rightarrow \omega_2' - k_2 v cos\theta_2, \tag{A.27}$$

where ω_i' $(i = 1, 2)$ is the non-shifted frequency. The detuning is then given by

$$\delta = (\delta_2' - k_2 v cos\theta_2) - (\delta_1' - k_1 v cos\theta_1). \tag{A.28}$$

With divergence present, the laser beam makes an angle with respect to the atomic beam given by

$$\theta_1' = \theta_1 + x \tag{A.29}$$
$$\theta_2' = \theta_2 + y \tag{A.30}$$

where x and y range from a minimum (x_1 and y_1) to a maximum (x_2 and y_2), which causes each angle to vary as well from θ_{min}' to θ_{max}'. For symmetry, $x_1 = -x_2$ and $y_1 = -y_2$. Now, detuning has been adjusted to account for these variations and given as

$$\delta = (\delta_2' - k_2 v cos(\theta_2 + y)) - (\delta_1' - k_1 v cos(\theta_1 + x)). \tag{A.31}$$

By using trigonometry identities and grouping terms, we find that

$$\delta = \delta' + k_2 v sin\theta_2 y - k_1 v sin\theta_1 x, \tag{A.32}$$

where δ' is the apparent resonance caused by the non-perfect orthogonality without divergence. Thus, the Raman resonance is now

$$I = \frac{\beta^2}{\beta^2 + (\delta' + k_2 v sin\theta_2 y - k_1 v sin\theta_1 x)^2}.$$

As expected, when x and y are 0, the intensity returns to its original Lorentzian form. We now carefully integrate over x and y to find the final equation for the intensity given as

$$\begin{aligned} I &= (\frac{1}{x_2 - x_1})\frac{1}{y_2 - y_1})(\frac{\beta^2}{2k_1k_2v^2sin\theta_1sin\theta_2}(\ln[(ay_2 + b)^2 + 1] + \ln[(ay_1 + c)^2 + 1] \\ &- \ln[(ay_2 + c)^2 + 1] - \ln[(ay_1 + b)^2 + 1] + 2(ay_1 + b)tan^{-1}(ay_1 + b) \\ &+ 2(ay_2 + c)tan^{-1}(ay_2 + c) \\ &- 2(ay_2 + b)tan^{-1}(ay_2 + b) - 2(ay_1 + c)tan^{-1}(ay_1 + c)), \end{aligned} \tag{A.33}$$

where,

$$\begin{aligned} a &= \frac{k_2vsin\theta_2}{\beta} \\ b &= \frac{\delta' - k_1vsin\theta_1x_2}{\beta} \\ c &= \frac{\delta' - k_1vsin\theta_1x_1}{\beta}. \end{aligned}$$

Equation A.33 is now the intensity profile for the atoms undergoing a Raman transition as a function of two photon detuning with both laser beam divergence and laser/atomic beam non-orthogonality taken into account. This function is plotted in Figure 5.6 for several values of the divergence angle.

THIS PAGE INTENTIONALLY LEFT BLANK

List of References

[1] I. Lachow, "The gps dilemma: Balancing military risks and economic benefits," *International Security*, vol. 20, no. 1, pp. 126–148, 1995.

[2] W. W. Chow, J. Gea-Banacloche, L. M. Pedrotti, V. E. Sanders, W. Schleich, and M. O. Scully, "The ring laser gyro," *Rev. Mod. Phys.*, vol. 57, pp. 61–104, Jan 1985. Available: https://link.aps.org/doi/10.1103/RevModPhys.57.61

[3] M. K. Gupta, I. A. Rasheed, V. A. Naidu, A. R. Rao, I. M. Chhabra, and S. Shankar, "Improvement in the bias of laser based optical rotational sensor by minimizing the lock-in due to surface roughness," in *AIP Conference Proceedings*, no. 1. AIP Publishing LLC, 2016, vol. 1728, p. 020645.

[4] J. Fang and J. Qin, "Advances in atomic gyroscopes: A view from inertial navigation applications," *Sensors*, vol. 12, no. 5, pp. 6331–6346, 2012.

[5] A. Meldrum, M. Manicchia, J. P. Davis, and F. A. Narducci, "Raman spectroscopy using a continuous beam from a 2d mot," in *Steep Dispersion Engineering and Opto-Atomic Precision Metrology XI*. International Society for Optics and Photonics, 2018, vol. 10548, p. 105481Y.

[6] M. O. Scully and J. P. Dowling, "Quantum-noise limits to matter-wave interferometry," *Physical Review A*, vol. 48, no. 4, p. 3186, 1993.

[7] P. G. Savage, "Blazing gyros: The evolution of strapdown inertial navigation technology for aircraft," *Journal of Guidance, Control, and Dynamics*, vol. 36, no. 3, pp. 637–655, 2013.

[8] D. W. Keith, C. R. Ekstrom, Q. A. Turchette, and D. E. Pritchard, "An interferometer for atoms," *Physical Review Letters*, vol. 66, no. 21, p. 2693, 1991.

[9] M. Kasevich and S. Chu, "Atomic interferometry using stimulated raman transitions," *Phys-ical Review Letters*, vol. 67, no. 2, p. 181, 1991.

[10] P. R. Berman, *Atom Interferometry*. Cambridge, MA, USA: Academic press, 1997.

[11] N. F. Ramsey, "Experiments with separated oscillatory fields and hydrogen masers," *Science*, vol. 248, no. 4963, pp. 1612–1619, 1990.

[12] M. Cadoret, E. De Mirandes, P. Cladé, S. Guellati-Khélifa, C. Schwob, F. Nez, L. Julien, and F. Biraben, "Combination of bloch oscillations with a ramsey-bordé interferometer: New determination of the fine structure constant," *Physical Review Letters*, vol. 101, no. 23, 230801, 2008.

[13] B. Canuel, F. Leduc, D. Holleville, A. Gauguet, J. Fils, A. Virdis, A. Clairon, N. Dimarcq, C. J. Bordé, A. Landragin *et al.*, "Six-axis inertial sensor using cold-atom interferometry," *Physical Review Letters*, vol. 97, no. 1, p. 010402, 2006.

[14] D. Keith, M. Schattenburg, H. I. Smith, and D. Pritchard, "Diffraction of atoms by a transmission grating," *Physical Review Letters*, vol. 61, no. 14, p. 1580, 1988.

[15] A. Miffre, M. Jacquey, M. Büchner, G. Trénec, and J. Vigué, "Atom interferometry," *Physica Scripta*, vol. 74, no. 2, p. C15, 2006.

[16] M. Manicchia, "Construction and characterization of a dual atomic beam accelerometer/gyroscope," Ph.D dissertation, Physics Dept., NPS, Monterey, CA, USA, 2020. Available: https://calhoun.nps.edu/handle/10945/65398

[17] A. Peters, K. Y. Chung, and S. Chu, "High-precision gravity measurements using atom interferometry," *Metrologia*, vol. 38, no. 1, p. 25, 2001.

[18] T. Gustavson, A. Landragin, and M. Kasevich, "Rotation sensing with a dual atom-interferometer sagnac gyroscope," *Classical and Quantum Gravity*, vol. 17, no. 12, p. 2385, 2000.

[19] H. J. Metcalf and P. Van der Straten, "Laser cooling and trapping of neutral atoms," *The Optics Encyclopedia: Basic Foundations and Practical Applications*, Wiley Online Library, 2007, p. 975.

[20] M. Manicchia, J. Lee, G. Welch, J. Mimih, and F. Narducci, "Construction and characterization of a continuous atom beam interferometer," *Journal of Modern Optics*, vol. 67, no. 1, pp. 69–79, 2020.

[21] N. Ramsey, *Molecular Beams*. Oxford University Press, 1956, vol. 20.

[22] K. Bergmann, H. Theuer, and B. Shore, "Coherent population transfer among quantum states of atoms and molecules," *Reviews of Modern Physics*, vol. 70, no. 3, p. 1003, 1998.

[23] U. Gaubatz, P. Rudecki, M. Becker, S. Schiemann, M. Külz, and K. Bergmann, "Population switching between vibrational levels in molecular beams," *Chemical physics letters*, vol. 149, no. 5-6, pp. 463–468, 1988.

[24] N. Vitanov, K. Suominen, and B. Shore, "Creation of coherent atomic superpositions by fractional stimulated raman adiabatic passage," *Journal of Physics B: Atomic, Molecular and Optical Physics*, vol. 32, no. 18, p. 4535, 1999.

[25] N. V. Vitanov, A. A. Rangelov, B. W. Shore, and K. Bergmann, "Stimulated raman adiabatic passage in physics, chemistry, and beyond," *Reviews of Modern Physics*, vol. 89, no. 1, p. 015006, 2017.

[26] P. Kumar, S. A. Malinovskaya, and V. S. Malinovsky, "Optimal control of population and coherence in three-level λ systems," *Journal of Physics B: Atomic, Molecular and Optical Physics*, vol. 44, no. 15, p. 154010, 2011.

[27] K. Fujii, "Introduction to the rotating wave approximation (rwa): Two coherent oscillations," *Journal of Modern Physics*, vol. 8, no. 12, pp. 2042–2058, 2017.

[28] J. R. Kuklinski, U. Gaubatz, F. T. Hioe, and K. Bergmann, "Adiabatic population transfer in a three-level system driven by delayed laser pulses," *Phys. Rev. A*, vol. 40, pp. 6741–6744, Dec 1989. Available: https://link.aps.org/doi/10.1103/PhysRevA.40.6741

[29] M. A. Kasevich, "Atom interferometry in an atomic fountain," *Ph.D. Thesis, Stanford University*, 1992.

[30] W. H. Louisell and W. H. Louisell, *Quantum Statistical Properties of Radiation*. Wiley New York, 1973, vol. 7.

[31] T. Begzjav, J. S. Ben-Benjamin, H. Eleuch, R. Nessler, Y. Rostovtsev, and G. Shchedrin, "Magnus expansion method for two-level atom interacting with few-cycle pulse," *Journal of Modern Optics*, vol. 65, no. 11, pp. 1378–1384, 2018.

THIS PAGE INTENTIONALLY LEFT BLANK

Initial Distribution List

1. Defense Technical Information Center
   Ft. Belvoir, Virginia

2. Dudley Knox Library
   Naval Postgraduate School
   Monterey, California